Polycrystalline Diamond Coating on Orthopaedic Implants: Realization, and Role of Surface Topology and Chemistry in Adsorption of Proteins and Cell Proliferation

Justas Zalieckas[1,], Ivan R. Mondragon[2], Paulius Pobedinskas[3,4], Arne S. Kristoffersen[1], Samih Mohamed-Ahmed[2], Cecilie Gjerde[2], Paul J. Høl[5,6], Geir Hallan[5,6], Ove N. Furnes[5,6], Mihaela Roxana Cimpan[2], Ken Haenen[3,4], Bodil Holst[1] and Martin M. Greve[1].*

1. Department of Physics and Technology, University of Bergen, Allegaten 55, Bergen, Norway

2. Department for Clinical Dentistry, University of Bergen, Årstadveien 19, Bergen, Norway

3. Institute for Materials Research (IMO), Hasselt University, Wetenschapspark 1, 3590 Diepenbeek, Belgium

4. IMOMEC, IMEC vzw, Wetenschapspark 1, 3590 Diepenbeek, Belgium

5. Department of Orthopaedic Surgery, Haukeland University Hospital, Jonas Lies vei 65, Bergen, Norway

6. Department of Clinical Medicine, University of Bergen, Jonas Lies vei 87, Bergen, Norway

KEYWORDS: diamond, surface wave plasma, orthopaedic implants, acetabular shell, collagen, albumin, cell proliferation

ABSTRACT: Polycrystalline diamond has the potential to improve the osseointegration of orthopaedic implants compared to conventional materials such as titanium. However, despite the excellent biocompatibility and superior mechanical properties, the major challenge of using diamond for implants, such as those used for hip arthroplasty, is the limitations of microwave plasma chemical vapor deposition (CVD) techniques to synthesize diamond on complex-shaped objects. Here, for the first time we demonstrate diamond growth on titanium acetabular shells using surface wave plasma CVD method. Polycrystalline diamond coatings were synthesized at low temperatures (~400 °C) on three types of acetabular shells with different surface structure and porosity. We achieved the growth of diamond on highly porous surfaces designed to mimic the structure of the trabecular bone and improve osseointegration. Biocompatibility was investigated on nanocrystalline diamond (NCD) and ultrananocrystalline diamond (UNCD) coatings terminated either with hydrogen or oxygen. To understand the role of diamond surface topology and chemistry in the attachment and proliferation of mammalian cells, we investigated the adsorption of extracellular matrix (ECM) proteins, and monitored the metabolic activity of fibroblasts, osteoblasts, and bone marrow-derived mesenchymal stem cells (MSCs). The interaction of bovine serum albumin (BSA) and Type I collagen with the diamond surfaces was investigated by confocal fluorescence lifetime imaging microscopy (FLIM). We found that the proliferation of osteogenic cells was better on hydrogen terminated UNCD than on the oxygen terminated counterpart. These findings correlated with the behaviour of collagen on diamond substrates observed by FLIM. Hydrogen terminated UNCD provided better adhesion and proliferation of osteogenic cells, compared to titanium, while growth of fibroblasts was poorest on

hydrogen terminated NCD and MSCs behaved similarly on all tested surfaces. These results open new opportunities for application of diamond coatings on orthopaedic implants.

1. INTRODUCTION

Conventionally used materials for medical implants are not ideal and come with limitations, which can lead to complications or even to a worst outcome: a revision surgery. The ideal biomaterial is expected to promote cellular growth, inhibit bacterial adhesion, and have excellent tribological properties. One of the most widely used materials for orthopaedic implants, such as for a hip replacement, is titanium and its alloys. However, lifetime of such implants is limited and, typically, ranges from 5 to 25 years. Revision surgeries are more complex, takes longer time, are more costly and have greater risk of complications. Typically, 4-5% of people who receive a hip implant may require revision surgery within 10 years and 15% of patients need revision surgery within 20 years [1]. The most common reasons for the failure of a titanium prosthesis are aseptic loosening and bacterial infection, both of which are directly related to the surface properties of titanium. This can be attributed to the fact that the surface of titanium has limited bioactivity and lacks anti-bacterial properties [2]. Therefore, much effort has been taken to improve the performance of titanium by various modifications and structuring of surface or by application of coatings [3]. Conventional materials suggested as coatings on titanium for enhanced biocompatibility include hydroxyapatite, bioactive glass, biphasic calcium phosphate and TiN. However, the stability, adhesion, and degradation performance of these coatings are still challenging [4, 5]. The drawbacks and limited performance can be partly attributed to the

quality and coverage of coatings which has a direct effect on responses such as initial cellular adhesion to a substrate, subsequent growth and proliferation, and bioactivity of material [6].

One of the most promising candidates to address the drawbacks of the state-of-the-art coatings is diamond. Diamond as a coating on orthopaedic implants provides several solutions due to its unique properties including wear resistance, high biocompatibility, corrosion resistance, chemical inertness, and high adhesion to titanium. All these properties, potentially, make diamond an ideal coating for orthopaedic implants overcoming the shortcomings of currently used solutions. It has been demonstrated that diamond coatings promote osteoblast adhesion [7-9], show anti-microbial properties [10, 11] and have a high degree of biocompatibility [12]. Moreover, diamond showed high tribological performance for coated femoral heads in a wear simulator [13] and has a high potential of being used also for wear-intense applications.

The standard method used for the growth of diamond on titanium substrate is chemical vapor deposition (CVD). Depending on the type of the energy source used to activate carbon-containing gas there are two most widely used CVD techniques: hot filament (HF) CVD and microwave plasma enhanced (MWPE) CVD with diamond films, typically, grown at substrate temperatures ranging from 500 °C to 1000 °C [14]. In HFCVD reactors gasses are activated by heated tungsten wires (filaments) while in the MWPECVD reactors microwave radiation is used as an energy source to generate a gas discharge. The HFCVD can achieve large area CVD but suffers from filament instability and contamination of the growing diamond film [15, 16]. Therefore, for the growth of high purity diamond films, typically, resonant-cavity MWPECVD systems operating at 2.45 GHz frequency are used. The deposition area of these systems is limited of up to approximately 30 cm^2 [17] by the gas discharge shape and size, which is roughly half the wavelength at a given frequency. These restrictions and planar-type nature of the above

listed techniques have limited the size and shape of the objects, which can be used for the synthesis of diamond. The current state-of-the-art is Rifai's et al. [18] demonstration of diamond deposition on additively manufactured hollow 3×3×3 mm^3 titanium cubes using MWPECVD method followed by the investigation of diamond synthesis on samples up to 8×8×3 mm^3 using a protective Faraday cage [19]. Maru et al. [13] used HFCVD method to deposit diamond on femoral heads 28 mm in diameter but did not study films uniformity.

As an alternative to HFCVD and resonant-cavity MWPECVD, either a distributed antenna array (DAA) [20] or a surface wave plasma (SWP) [21, 22] CVD system could be used for diamond synthesis even at temperatures below 100 °C [23]. These two techniques operate at low pressures (<2 mbar) and yield larger gas discharge volumes compared to HFCVD and MWPECVD methods, which is beneficial for diamond growth on complex-shaped objects. The latest demonstrations come from Dekkar et al. [24] showing diamond growth on cylindrical-shape titanium implant of 6.3 mm height with DAA CVD system and Varga et al. [25] achieving non-uniform growth on copper rods 2.5 mm in diameter and approximately 30 mm in length using SWP CVD. Therefore, there is a need to investigate diamond synthesis on larger than above mentioned objects to facilitate the use of diamond-based materials for orthopaedic implants such as a hip replacement.

Surface topology and chemistry of diamond coatings plays an important role in adsorption of proteins and cells proliferation and viability. Alcaide et al. [26] showed that the topology and doping of polycrystalline diamond films alter the adsorption of serum proteins and can influence the resistance of fibroblasts adhesion and proliferation. Cytotoxicity evaluation of fibroblasts on diamond coatings showed no induced cytotoxic response [27]. Liskova et al. [28] found that osteoblasts exhibited higher growth rate on oxygen terminated diamond films compared to

hydrogen terminated counterparts. Furthermore, they found that oxygen terminated surface supports the deposition of extracellular matrix proteins. A recent study from Rifai [29] shows that polycrystalline diamond promotes expression of adhesion proteins, and that surface topology can guide the proliferation of osteoblasts. As suggested by Fong et al. [6] mesenchymal stem cells (MSCs) can be integrated on diamond coatings to improve osteoconductive properties of implants, however, the literature within the field reports inconsistent findings of MSC adhesion and proliferation on diamond [30]. Therefore, it is important to study multiple cell types to gain a better understanding of cell adhesion and proliferation on diamond substrates.

Here, for the first time, we use SWP CVD method to synthesize diamond on complex-shaped orthopaedic implants, namely titanium acetabular shells, taken from patients after revision hip replacement surgeries. The biocompatibility and properties of the films were investigated on two types of coatings, nanocrystalline diamond (NCD) and ultrananocrystalline diamond (UNCD), deposited on silicon wafers and titanium hemispheres designed to mimic the shape of the acetabular shells. We evaluated the metabolic activity of fibroblasts, osteoblasts and MSCs on NCD and UNCD surfaces terminated with hydrogen and oxygen showing that proliferation and viability of MSCs is best on hydrogen terminated UNCD. Furthermore, we show that hydrogen terminated UNCD provides better adhesion and proliferation for osteogenic cells, compared to titanium substrate. Lastly, for the first time, we complement biocompatibility assessment of the cells with the investigation of adsorption of blood and extracellular matrix (ECM) proteins on diamond surface. We show that Type I collagen adsorption and behaviour observed by confocal fluorescence lifetime imaging microscopy (FLIM) correlates with proliferation of MSCs and osteogenic cells on hydrogen and oxygen terminated UNCD.

2. EXPERIMENTAL SECTION

2.1. Synthesis of Polycrystalline Diamond.

2.1.1. Sample Preparation. Polycrystalline diamond was synthesized on three hemispherical acetabular shells taken from patients after revision hip replacement surgeries and donated by Haukeland University Hospital in Bergen, Norway. The bulk of all acetabular shells is made from Ti-6Al-4V alloy with the following types of backing material: i) porous metal made from trabecular-type tantalum material, referred to as "TRABECULAR" (Cat. No. T/TA 6202-58-20, Trabecular metal modular, Zimmer, d = 58 mm), ii) fiber mesh made from commercially pure (CP) titanium, referred to as "M-MESH" (Cat. No. T6610-54-02, Harris Galante II, Zimmer, d = 54 mm), and iii) arc-deposited plasma sprayed CP titanium, referred to as "TRIDENT" (Cat. No. 500-01-58F, Trident, Stryker, d = 58 mm). The residual bone content on acetabular shells was mechanically brushed away in a warm water (50-70 °C) followed by ultrasonication in acetone for 30 min. Uniformity of diamond coatings was investigated on hemispheres 40 mm and 60 mm in diameter machined from Ti-6Al-4V alloy and polished using high-capacity finisher (Radiance 50, Schmidts Polérmedel).

2.1.2. Diamond Coating. Prior to deposition all samples were exposed for 3 min *ex-situ* to a reactive oxygen gas plasma to achieve good nanodiamond (ND) seeding density using the same process conditions as in Refs [31, 32]. The acetabular shells and titanium hemispheres were seeded by pouring water-based colloidal solution of ultra-dispersed ND particles (5-7 nm in diameter) over them and rinsing them afterwards with deionized water. Silicon substrates (polished 4-inch wafers) were seeded with the same ND suspension via drop casting and

subsequent spin-drying as detailed in Ref [33]. Polycrystalline diamond samples were prepared by SWP CVD (W&L Coating Systems, TruDi MWPECVD System) keeping all samples 2.5 cm away from the linear antenna (LA). A CVD gas mixture consisting of 2% methane (CH_4), 6% carbon dioxide (CO_2) and 92% hydrogen (H_2) was used to grow NCD films while UNCD films were synthesized using 8% CH_4, 6% CO_2 and 86% H_2. Carbon dioxide was added to ensure effective etching of *sp2* carbon phases at low temperatures [34, 35]. The NCD and UNCD films were grown for 22 h and 10 h, respectively. Both types, NCD and UNCD films, were deposited on titanium hemispheres and silicon wafers while only NCD was synthesized on acetabular shells. The temperature of the samples 2.5 cm away from the LA was measured to be ~400 °C. The microwave power, gas pressure and total gas flow were 2800 W, 0.22 mbar, and 150 sccm, respectively.

2.1.2. Surface Treatment. The silicon wafers were cut into smaller samples and divided into two batches. Samples from the first batch were terminated with hydrogen by exposing them to hydrogen plasma inside the in-house built MWPECVD reactor for 10 min at 600-700 °C and 50 mbar keeping microwave power at 1400 W. A reactive ion etcher Plasmatherm 790+ was used to terminate the samples from the second batch with oxygen. The samples were placed on the grounded holder and exposed to oxygen plasma at 0.133 mbar pressure at room temperature for 2 min with no added bias, keeping the power at 100 W.

2.2. Material Characterization.

The surface morphology of the polycrystalline diamond films was examined with Raith e-Line and Zeiss SUPRA 55VP scanning electron microscopes (SEM), using inlens secondary electrons detectors and an acceleration voltage of 10 kV. Surface topology and roughness were

investigated with Bruker Dimension Icon atomic force microscope (AFM), employing peak force tapping mode (ScanAsyst) with a ScanAsyst-Air probe (Bruker). Film thickness was measured using spectral reflectance technique with Filmetrics F10-RT reflectometer.

The composition of the diamond films was examined by Raman spectroscopy measuring spectra in 1000-2000 cm^{-1} range with a HORIBA LabRAM 800 HR spectrometer working in a confocal mode and using a 488 nm wavelength Ar laser as an excitation source. The chemical composition of the coated surfaces was investigated with Axis Ultra DLD (Kratos Analytical) X-ray photoelectron spectrometer (XPS). High-resolution XPS spectra were taken by probing of 700 × 300 μm^2 areas using a monochromatic Al Kα X-ray source operating at 10 kV and 10 mA. Survey and regional scans were acquired with pass energy of 160 eV and 20 eV, respectively. The step size was set to 1 eV for the survey and 0.1 eV for regional scans. The reported spectra were charge corrected with reference to adventitious carbon (C 1s peak at 284.8 eV). Acquired data were analyzed using CasaXPS (Casa Software Ltd).

The surface wettability of titanium and diamond samples was characterized with a video-based optical contact angle measurement system OCA20 LHT (Dataphysics) by measuring the static water contact angle. The contact angles were measured at room temperature by gently depositing water droplets having a volume of 3 μL. The measurements on diamond surfaces were done within 15 min after the plasma treatment (see Section 2.1.2) to avoid surface contamination by hydrocarbons and change of wetting angles [31].

2.3. Adsorption of Proteins.

2.3.1. Sample Preparation. Bovine serum albumin (BSA) and Type I collagen (COL) from bovine skin, both labeled with fluorescein isothiocyanate (FITC), were purchased from Sigma-

Aldrich. Silicon samples with hydrogenated and oxygenated NCD and UNCD were immersed in BSA (1 mg/ml in 10 mM Tris buffer at pH 7.4) and COL (1 mg/ml in 0.01 M acetic acid at pH 5.0) solutions for 1 h at room temperature. Subsequently, samples were rinsed 3 times and submerged in 10 mM Tris buffer at pH 7.4 prior to the fluorescence lifetime measurements.

2.3.2. Fluorescence Lifetime Imaging Microscopy (FLIM). Fluorescence lifetime data of BSA^{FITC} and COL^{FITC} conjugates were obtained using time-correlated single-photon counting (TCSPC). A Ti:Sapphire laser (Coherent Chameleon Ultra) tuned to 900 nm wavelength, generating femtosecond pulses (pulse width 140 fs) at an 80 MHz repetition rate (12.5 ns between each pulse) was used for two-photon excitation of the samples. Excitation light was guided to confocal inverted microscope (Leica TCS SP5) and focused by a water immersion objective (NA = 1.2). The samples were scanned at a line frequency of 400 Hz and fluorescence of FITC was detected by a built-in photomultiplier tube (PMT) in a range of 500-700 nm. Line, frame, and pixel clock signals were generated and synchronized by a Hamamatsu R3310-02 PMT detector and linked via a TCSPC imaging module (SPC-830, Becker-Hickl) to generate fluorescence lifetime data. The fluorescence lifetime data for each sample was collected by scanning 110 × 110 μm^2 area with the spatial resolution of 128 × 128 pixels. The collected photons for each pixel were stored as a histogram (decay trace). We used a bi-exponential decay model convoluted with the instrument response function (IRF) to represent the data of each pixel. To increase the signal-to-noise ratio, for each pixel 8 × 8 decay traces of the neighboring pixels were summed and the fluorescence lifetimes (τ_1 and τ_2) for the central pixel were obtained from the Maximum-Likelihood fit to the summed decay trace using SPCImage software, hence obtaining a decay matrix (128 × 128 pixels) for each tested sample.

2.4. Cell Growth on Diamond-Coated Substrates.

2.4.1. Cells and cultivation. Human bone marrow-derived mesenchymal stem cells (BMSCs) were isolated from 2 donors, a 53 years old male (BMSCmax) and a 59 years old female (BMSCbeh), under ethical approval from the Regional Committee for Medical and Health Research Ethics in Norway (approval number: REK vest 7199). BMSCs were characterized based on the expression of a set of cell surface markers (CD34, CD45, CD73, CD90, CD105 and HLA-DR). BMSCs were cultured at a seeding density of 5×10^3 cells/cm^2 using culture medium Minimum Essential Medium - Alpha Modification (αMEM, Thermo Fisher Scientific) supplemented with 10% fetal bovine serum (FBS, Sigma-Aldrich) and 1% antibiotics (penicillin/streptomycin, Sigma-Aldrich). Human primary lung fibroblasts (Innoprot) were cultured in fibroblast medium (Innoprot) at a seeding density of 6×10^3 cells/cm^2. The osteosarcoma cell line Saos-2 (DSMZ) was cultured at a seeding density of 1.2×10^4 cells/cm^2 in McCoy's 5a medium (Thermo Fisher Scientific) supplemented with 15% FBS, GlutaMAX™ (Thermo Fisher Scientific) and 1% antibiotics. All cells were maintained in a humidified incubator with 5% CO_2 at 37 °C. The medium was changed twice a week and cells were sub-cultured when reaching 70-80% confluency. For experiments, BMSCs and fibroblasts were used at passages 3-6, while Saos-2 at passages 6-9.

2.4.2. Cell viability/proliferation assay. Diamond-coated silicon wafers were cut in 1.8×4.5 cm^2 strips and surface treated as described in Section 2.1.2. Titanium sheet 0.52 mm in thickness (TI010450/10, GoodFellow) was polished as described in Section 2.1.1 and cut in 1.8×5.0 cm^2 strips. The strips were ultrasonicated in acetone for 30 min and then immersed in 70% ethanol for 10 min and air-dried inside a laminar flow hood. The sterile strips were stuck to the bottom of a black, bottomless 96-well plate (ProPlate MP™, Grace Bio-Labs). The wells were rinsed twice with sterile water and let air-dry while preparing cell suspensions in culture medium. Before

seeding, cell suspensions were mixed 1:1 with medium containing 2X RealTime-Glo™ MT Cell Viability Assay (Promega) following manufacturer's instructions. Cells were seeded at the following densities in duplicate wells; 9350, 7800 and 12 500 cells/cm^2 for BMSCs, fibroblasts and Saos-2, respectively. Upon cell seeding, luminescence was measured at different time points (0, 1, 2, 4, 8, 24 and 48 h) using a microplate reader (SkanIt™, Thermo Fisher Scientific) equipped with a temperature control module (37 °C). Three independent experimental repetitions were performed for each cell line. The data shown is normalized to luminescence at time 0 h.

2.4.3. *Immunostaining and fluorescence microscopy*. Titanium sheet and diamond-coated silicon wafers were cut in 2.2 × 2.2 cm^2 squares. The diamond films were terminated with hydrogen and oxygen as described in Section 2.1.2. The substrates were sterilized in 70% ethanol for 10 min and air-dried inside a laminar flow hood. The substrates were adhered to the bottom of a re-usable 8-well silicon insert (flexiPERM®, Heraeus Instruments). Cells were seeded at the densities stated in Section 2.4.1 and cultured for 5 days. The medium was changed every second day and at day 5 cells were fixed with 4% paraformaldehyde for 15 min. Cells were then permeabilized with 0.2% Triton X-100, blocked with 4% BSA/4% FBS and incubated overnight at 8 °C with mouse anti-vinculin antibody (clone hVIN-1, Sigma-Aldrich). The anti-vinculin antibody was detected with goat anti-mouse antibody-AlexaFluor 488 (Thermo Fisher Scientific). Cells were counter-stained with DAPI and Phalloidin-Atto 565 (Sigma-Aldrich). Finally, substrates containing the stained cells were mounted on #1.5 glass coverslips using Mowiol® (Sigma-Aldrich) mounting media. Specimens were imaged using a TCS SP8 confocal microscope (Leica Microsystems) equipped with hybrid detectors, White and Blue diode lasers and a 40× immersion objective (NA = 1.1). Whole volume images of the cells were acquired with a *z*-step of 0.5 μm.

2.4.4. *Image analysis*. Nucleus area and nucleus aspect ratio were used to indirectly analyze cell attachment, shape and expansion; the larger the nucleus area, the larger the cell's cytoskeleton expansion and thus better attachment. Concerning aspect ratio, a value of 1 indicates a perfect circle while values larger than 1 describe an elongated circle (oval shape). The shape of the nucleus often correlates with the overall shape of the cell [36-39]. The open-source software Fiji [40] was used to quantify number of cells, nucleus area and nuclei aspect ratio at day 5 of culture onto the different substrates. Automated analysis was performed on the DAPI channel (nuclei staining) as follows; images were processed to obtain a *z*-projection based on maximum intensity, global thresholding applied for binarization (value set to 50), holes filled and the images segmented using a watershed algorithm. Finally, particles were counted and analyzed using the Analyze Particles tool with a minimum particle size of 120 μm^2. A total of ten images (*z*-projections) were analyzed for each cell type/substrate combination, except for fibroblasts plated on hydrogenated UNCD, where 20 images were used due to the low cell number. The total number of cells analyzed is specified in the respective plots and was higher than 250, except for fibroblasts.

2.4.5. *Statistical analysis*. The IBM© SPSS© Statistics v27 was used to obtain descriptive statistics data, perform normality analysis (Kolmogorov-Smirnov and Shapiro-Wilk tests) and generate box-plots. One-way ANOVA with Bonferroni post-hoc test was performed on normally-distributed samples. Non-normal data (fibroblasts on hydrogenated substrates) were analyzed with Kruskal-Wallis test for pairwise comparisons. The significance level is $p \leq 0.05$.

3. RESULTS AND DISCUSSION

We synthesized polycrystalline diamond on acetabular shells with three different surface structures and porosities and investigated diamond films properties on titanium hemispheres, machined to mimic the shape of the shells. The role of surface topology and chemistry of diamond in adsorption of proteins is studied by time-resolved fluorescence microscopy based on excited state lifetimes of FITC conjugates with BSA and collagen. Biocompatibility of diamond films was assessed by observing the metabolic activity of fibroblasts, osteoblasts, and MSCs. The role of ECM proteins in cell proliferation on diamond is investigated by measuring behavioural changes of adsorbed collagen.

3.1. Polycrystalline Diamond Coating on Acetabular Shells and Titanium Hemispheres.

Figure 1a shows a schematic drawing of the linear antenna SWP CVD system used to synthesize diamond at ~400 °C. The titanium hemispheres (Figure 1b) and acetabular shells (Figure 1c) were placed within the so called "CVD region" [41, 42], which can extend up to 20 cm from the antennas, to achieve homogeneous CVD of diamond. Figure 1b shows a titanium hemisphere 60 mm in diameter coated with NCD. The thin film interference pattern visible in the lower part of the sample indicates non-uniform thickness of the film extending up to the hemispherical part. Figure 1c shows SEM micrographs of uniform NCD coating on TRABECULAR, M-MESH and TRIDENT acetabular shells. The TRABECULAR mimics the structure of the trabecular bone and has up to 80% porosity with the average pore size of ~400 μm. The porous structure of the shell makes seeding and, as a result, diamond CVD challenging. From SEM micrographs (Figure S1, Supporting Information) we estimated that NCD was deposited on porous tantalum structures down to a depth of 600-800 μm. For the M-MESH the NCD film uniformly covers the surface of titanium fibers ~300 μm in diameter except for some random regions of fibers intercrossing. The coatings in these regions do not fully cover the implant surface (Figure S1, Supporting

Information), which can be explained by lower ND seeding density. The TRIDENT is an arc-deposited titanium shell with lower porosity and smaller pore size (30-100 μm) compared to the TRABECULAR shell. The NCD coating on the TRIDENT is smooth and covers most of the investigated surface area except of few random voids present in regions of high granularity, (Figure S1, Supporting Information), which can be attributed to the variations of the seeding density due to the size of the pores and surface roughness.

Figure 1d shows the background corrected Raman spectra of NCD films grown on TRABECULAR, M-MESH, and TRIDENT acetabular shells. The characteristic diamond peak (D band) is observed at 1332 cm^{-1} and a broad line shape (G band) is visible at around 1580 cm^{-1}. The broad peaks clearly visible near 1190 cm^{-1} and at around 1480 cm^{-1} are assigned to transpolyacetylene segments at grain boundaries and represents a signature of NCD [43-45]. The amount of *sp3* bonded carbon in NCD coatings is estimated to be 49.4%, 35.7% and 44.1% for TRABECULAR, M-MESH and TRIDENT, respectively using the method detailed in Ref [17].

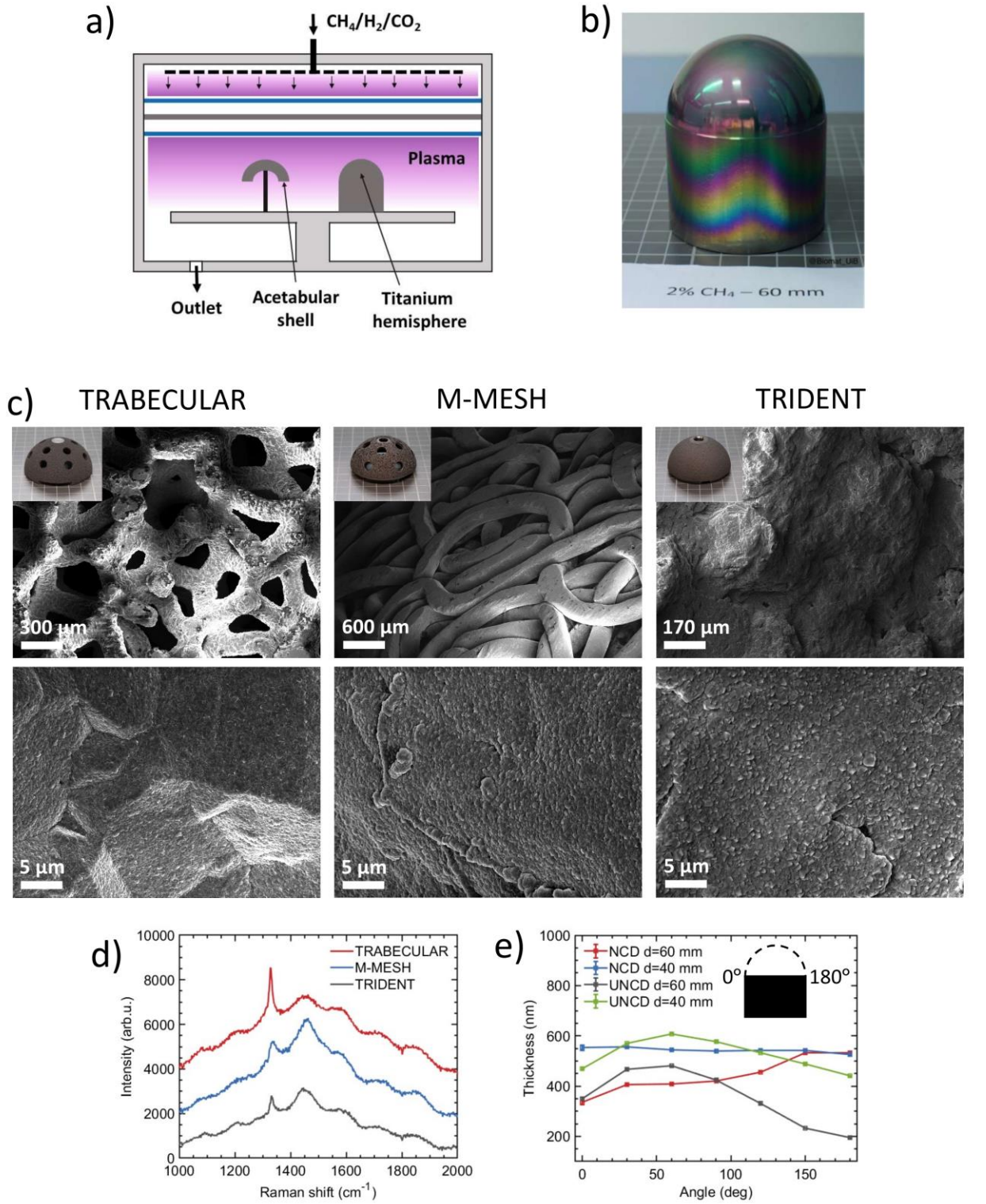

Figure 1. (a) Schematic drawing of the surface wave plasma chemical vapor deposition (SWP CVD) system. (b) titanium hemisphere 60 mm in diameter coated with nanocrystalline diamond (NCD). (c) Scanning electron micrographs of NCD coating on TRABECULAR, M-MESH, and TRIDENT acetabular shells. The insets show photographs of the acetabular shells after CVD.

(d) The background corrected Raman spectra of NCD films grown on acetabular shells. (e) Thickness profiles of NCD and ultrananocrystalline diamond (UNCD) films grown on titanium hemispheres.

The uniformity of diamond coatings was investigated on titanium hemispheres, since thickness measurements of thin films on porous surfaces is challenging. Figure 1e shows thickness profiles along titanium hemispheres 60 mm and 40 mm in diameter for NCD and UNCD films. The mean thickness for 40 mm in diameter hemisphere is 543 nm (526 nm) for NCD (UNCD) and 441 nm (355 nm) for 60 mm counterpart for NCD (UNCD). The uniformity of NCD on 40 mm in diameter hemisphere is 2.8% and drops to 22.3% with diameter increased up to 60 mm. The poor uniformity of UNCD coatings can be attributed to the drift of the surface waves on the linear antenna during CVD process. This hypothesis is supported by the similarity of thickness profiles for both hemispheres, hence indicating a systematic effect. We observed that granularity of NCD films changes with distance from the top (at 90 °, see Figure 1e) to the bottom (at 0 °, see Figure 1e) of the hemispheres: for 40 mm in diameter hemisphere the average grain size decreases from 334 ± 46 nm to 241 ± 59 nm, while for 60 mm from 265 ± 42 nm to 135 ± 31 nm (Figure S2, Supporting Information). This can be explained by decreasing plasma density with the distance from the antenna [42]: increasing the diameter of the hemisphere increases the difference in plasma density at the top and at the bottom of the hemisphere, thus yielding a larger difference of the average grain size.

The uniformity of coatings on porous meshes might be improved by improving the uniformity and density of pre-seeding of the substrates. One possible option for nucleation enhancement would be to use adamantane seeding instead of ND as suggested by Tsugawa et al. [46]. Another possibility comes from Tsugawa et al. [23] study where they observed that diamond nucleation rate increases with decreasing substrate temperature and suggested that at certain conditions

diamond nucleation takes place in the gas phase. In this way nucleated diamond in a plasma could diffuse towards the substrate, penetrate inside porous structures finally precipitating on them and yielding more uniform coating.

3.2. BSA and Collagen Adsorption on NCD and UNCD coatings. We investigate adsorption of proteins on NCD and UNCD films grown on silicon substrates using the same conditions as for the synthesis of diamond on acetabular shells and titanium hemispheres (Figure S3, Supporting Information). Figures 2a and 2b show high resolution AFM images of NCD and UNCD films topography on silicon substrates, respectively. The root-mean-square (RMS) roughness of the surface was measured to be 51 nm (10 nm) for NCD (UNCD) films. Figure 2c shows 1D profiles of surface topology scans depicted in Figure 2a and 2b indicating fivefold difference between roughness of NCD and UNCD films tested. The contact angle indicating wettability of the surfaces was measured to be 70.4 ± 3.0° and 64.9 ± 3.1° for hydrogenated NCD (NCD-H) and UNCD (UNCD-H), respectively as well as 9.9 ± 0.5° and 11.0 ± 3.4° for oxygenated NCD (NCD-O) and UNCD (UNCD-O), respectively.

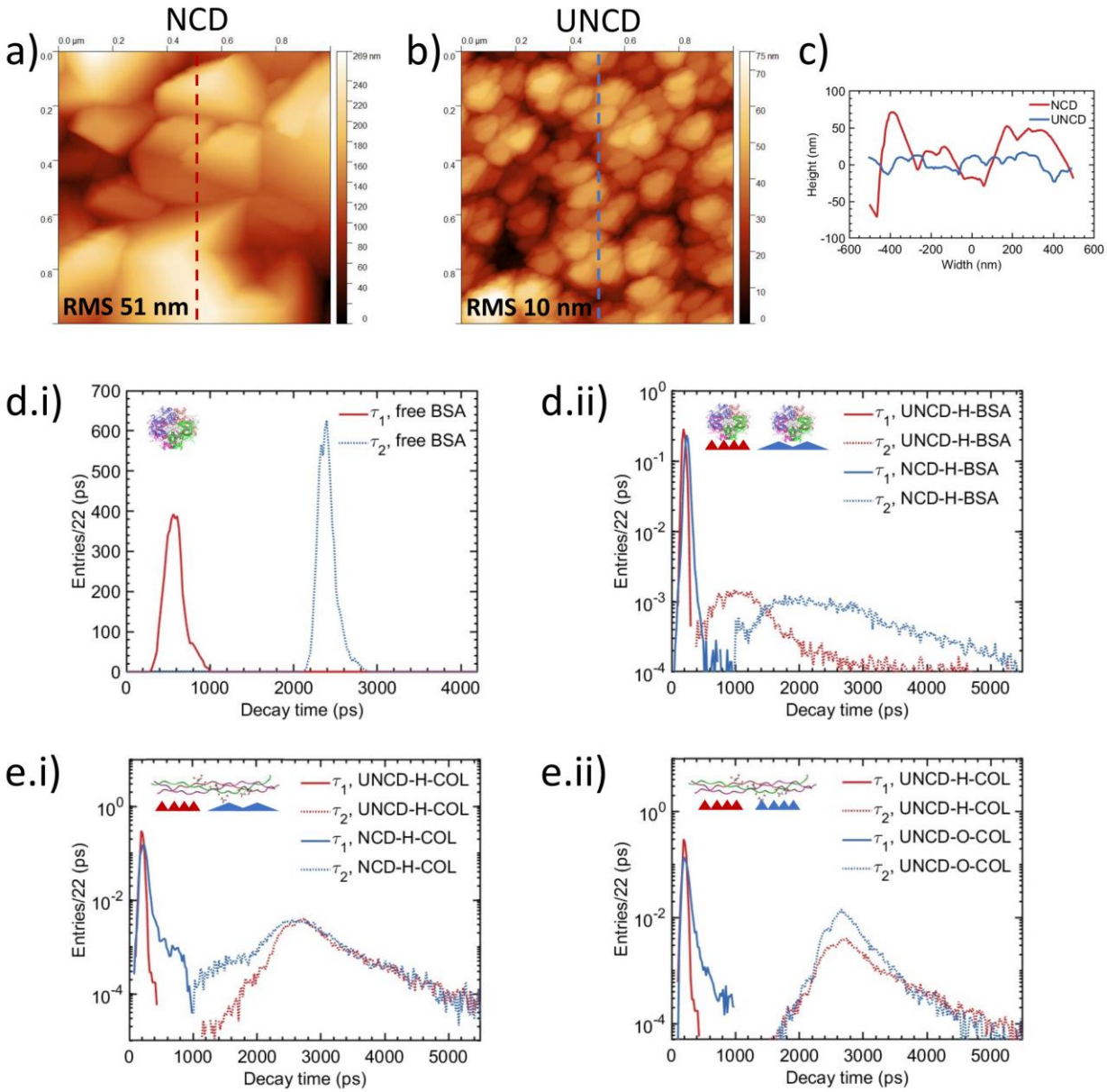

Figure 2. High resolution atomic force microscopy images of (a) nanocrystalline diamond (NCD) and (b) ultrananocrystalline diamond (UNCD) films topography on silicon substrates. (c) 1D profiles of surface topology scans shown as dashed red and dashed blue lines in (a) and (b), respectively. (d.i) Weighted histograms of fluorescence lifetimes τ_1 and τ_2 of bovine serum albumin and fluorescein isothiocyanate (BSA^{FITC}) conjugates in 10 mM Tris buffer at pH 7.4. (d.ii) Normalized and weighted histograms of fluorescence lifetimes τ_1 and τ_2 of BSA^{FITC} adsorbed on hydrogenated UNCD and NCD films. (e.i) Normalized and weighted histograms of fluorescence lifetimes τ_1 and τ_2 of collagen fluorescein isothiocyanate (COL^{FITC}) conjugates adsorbed on hydrogenated UNCD and NCD films, and on (e.ii) oxygenated UNCD and NCD films.

First, we investigate BSA^{FITC} conjugates in 10 mM Tris buffer at pH 7.4. Figure 2d.i shows weighted histograms of fluorescence lifetimes τ_1 and τ_2 obtained from the decay matrix (128 × 128 pixels). Each entry in the histogram $\tau^i_{1,2}$ is weighted by the corresponding decay time fraction $a^i_{1,2}$ extracted from the fit to a decay trace for a given pixel in the decay matrix. Both distributions are normally distributed, and yields mean lifetimes of τ_1 = 0.59 ns and τ_2 = 2.42 ns. The fluorescence lifetime of fluorescein reported in literature τ_{FITC} = 3.7-4.1 ns [47] is longer compared to the longest obtained lifetime τ_2. The shorter decay lifetime of BSA^{FITC} conjugate can be explained by dynamic self-quenching of the excited fluorophore in the encounter complex with monomer in the ground state, accelerated by fluorescence resonance energy transfer (FRET) [47]. Furthermore, FITC is bound to BSA through the ε-amino group of lysines of the albumin with 7 to 12 fluorophores decorating each protein. High labeling ratios yield shorter dye-to-dye distances and, hence shortening of average lifetimes [48]. We found from the goodness of the fits that two lifetime components are sufficient to describe fluorescence decay of BSA^{FITC} conjugates. The longer lifetime (τ_2) was attributed to the outermost fluorophores on albumin while intermediate and locally concentrated FITC-FITC pairs were assigned to the shorter lifetime (τ_1).

Figure 2d.ii shows normalized and weighted histograms of fluorescence lifetimes τ_1 and τ_2 of BSA^{FITC} conjugates adsorbed on UNCD-H and NCD-H films. The distributions of τ_2 are centered at around 1 ns and 2 ns for UNCD-H and NCD-H, respectively and have broader line shapes compared to τ_2 distribution for albumin in a solution. The mean value of τ_1 is 0.21 ns for UNCD-H and 0.25 ns for NCD-H. Since BSA undergoes irreversible structural changes upon adsorption on hydrophobic surface [49] the broadening of τ_2 distributions can be attributed to

changes in distances of the outermost fluorophores relative to each other and relative to fluorophores associated to τ_1. On UNCD-H (NCD-H) surface the difference in electronegativity between hydrogen (2.1) and carbon (2.5) produces H-C dipoles with +0.05*e* at surface of hydrogen yielding effective electric surface charge density of up to 1×10^{14} cm^{-1} [50]. The H-C dipoles provides sites for negatively ionized residues (ASP and GLU) of albumin with the total charge of approximately -9*e* at pH 7.2 [51], hence inducing conformational changes, which in turn affects excitation lifetimes. Our findings of τ_2 shortening for smoother UNCD-H surface compared to NCD-H surface agrees with results from Handschuh-Wang et al. [47] showing that fluorescence lifetime of BSA^{FITC} adsorbed on polycrystalline diamond decreases with decreasing diamond grain size. The shortening of τ_1 is attributed to surface-induced fluorescence quenching of fluorophores interacting with the diamond surface and changes in dye-to-dye distance due to conformational changes of BSA. These results show that topology and hydrophobicity of diamond surface can be used to affect conformational behavior of BSA upon adsorption. Since albumin is one of the most abundant proteins and adsorb immediately after implantation from blood and biological fluids, control over albumin adsorption on diamond coating might be used to tailor the integration of orthopaedic implants.

Figure 2e.i shows normalized and weighted histograms of fluorescence lifetimes τ_1 and τ_2 of COL^{FITC} conjugates adsorbed on UNCD-H and NCD-H films. The distributions of τ_2 have broad line shapes and are centered at around 2.6 ns. Collagen is decorated on average with one fluorophore, which yields longer dye-to-dye distances compared to BSA^{FITC} conjugates and, hence longer lifetimes of τ_2. Collagen at pH 7.2 assembles into fibrillar structures, typically, forming a confluent monolayer on the substrate [52]. Therefore, fluorophores can be distributed radially and be exposed to a solution, a diamond surface or to neighboring amino acids. We

attribute lifetime τ_2 to fluorophore interaction with solution and neighboring proteins. Similarly, as for the BSA^{FITC}, lifetime τ_1 is attributed to surface-induced fluorescence quenching of fluorophores interacting with the diamond surface. The distribution of lifetime τ_1 for NCD-H has a broader right-hand side tail compared to one for UNCD-H. Broadening of the distributions can be explained by topological differences between the two surfaces and size of the collagen. Collagen consists of tropocollagen molecules ~300 nm in length with diameters of ~1.5 nm, leading to high aspect ratio of ~190 [53]. Higher roughness of NCD-H surface (see Figure 2) given the length of collagen might increase the distance between fluorophores, residing on the fibrils and the surface, thus reducing fluorescence quenching and yielding broader distributions.

Figure 2e.ii shows distributions of lifetimes τ_1 and τ_2 of COL^{FITC} conjugates adsorbed on UNCD-H and UNCD-O films. The distributions of τ_2 have similar line shapes and are centered at around 2.6 ns. The right-hand side tail of τ_1 distribution for UNCD-O is broader compared to one for UNCD-H and cannot be a result of surface topology of the substrates. Cole et al. [54] investigated the adsorption of a collagen fragment on hydrogen terminated and natively oxidized silicon surface using all-atom molecular dynamics. They found that within 5 ns collagen might be highly mobile on the hydrophilic surface while on hydrophobic surface it remains adsorbed more stably and maintains its helical structure. Therefore, we attribute the broadening of τ_1 distribution for UNCD-O to a higher mobility of collagen on hydrophilic diamond surface. These results show that adsorption of collagen on diamond surface is affected by surface topology and wettability. Since collagen constitutes the major component of ECM and can promote adhesion and proliferation of MSCs [55], control of collagen adsorption by tailoring diamond surface and chemistry might be beneficial for enabling better integration of implants into existing bone via stem cell recruitment and bone regeneration [6].

3.3. Cell attachment and proliferation. Next, we sought to investigate the interaction and growth of primary adult fibroblasts, the osteogenic cell line Saos-2 and BMSCs, all from human origin, onto diamond films and bare titanium as the reference material. For simplicity, we only show results for BMSC from one donor (BMSCmax) in the main text while results for other donor (BMSCbeh) can be found in Supporting Information. Figure 3a shows the evolution in luminescence signal as a measurement of increasing metabolic activity, which includes cell growth and division, of living cells over time. We observed that UNCD-H outperformed its oxygen terminated counterpart and NCD films regarding the support of cell growth of fibroblasts and BMSCs over the whole 48 h incubation time. In addition, fibroblasts and BMSCs seeded on UNCD-H films exhibited growth profiles close or slightly better than those observed on titanium (Figure 3a). For Saos-2, all diamond films, except UNCD-O, performed equally well and close to the growth profile seen on titanium (Figure 3a). Notably, metabolic activity during the first 4 h of culture, which reflects cell attachment, of BMSCs and Saos-2 was considerably higher on hydrogen terminated UNCD and NCD films compared to oxygen terminated counterparts and even to titanium (Figure S4, Supporting Information). This suggests that hydrogen terminated diamond films facilitate adsorption of cell attachment factors (e.g., ECM proteins like collagen) present in the cell culture medium and secreted by the cells. However, this was not the case for fibroblasts; the initial cell attachment process was similar in all substrates except for NCD-H, where fibroblasts attached poorly.

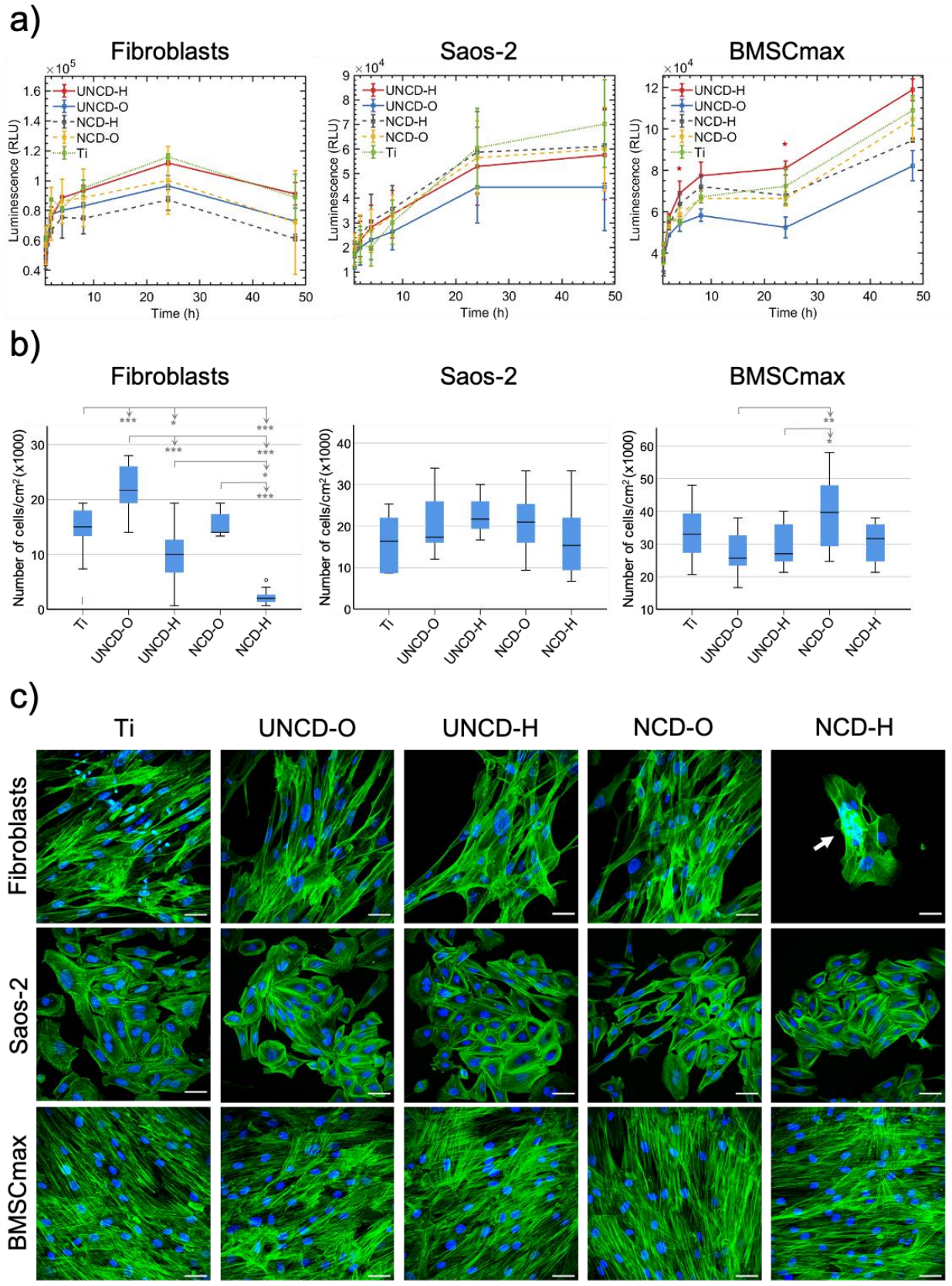
a)
Fibroblasts
Saos-2
BMSCmax
UNCD-H
UNCD-O
NCD-H
NCD-O
Ti
Luminescence (RLU)
Time (h)
b)
Fibroblasts
Saos-2
BMSCmax
Number of cells/cm² (x1000)
Ti
UNCD-O
UNCD-H
NCD-O
NCD-H
c)
Ti
UNCD-O
UNCD-H
NCD-O
NCD-H
Fibroblasts
Saos-2
BMSCmax

Figure 3. Growth of fibroblasts, osteogenic cells (Saos-2) and bone marrow-derived mesenchymal stem cells (BMSCmax) on titanium and diamond-coated substrates. (a) Evolution in luminescence signal as a measurement of increasing metabolic activity. (b) Number of cells per cm^2 at day 5 of culture. Statistical annotations: `*´ 0.05>p>0.01, `´ 0.01>p>0.001, `***´ p<0.001 (c) Fluorescence micrographs of cells fixed at day 5 and stained with phalloidin-ATTO 565 (green) and DAPI (blue) to visualize actin filaments (F-actin) and nuclei, respectively. Shown are maximum z-projections of merged phalloidin-ATTO 565/DAPI. Arrow points to a densely packed cell cluster. Scale bars are 50 µm.*

To further validate these observations, we carried out microscopic analysis of the three cell types cultured for 5 days on diamond-coated films and titanium. As illustrated in Figure 3b-c and Figure S5 (Supporting Information), BMSCs seemed to grow equally well on all surfaces after 5 days of culture; BMSCs were able to form confluent monolayers of elongated cells with fully developed filamentous (F)-actin bundles (i.e., stress fibers) across the cytoplasm. In fact, the number of BMSCmax present at day 5 was higher on NCD-O than on any of the other substrate (Figure 3b), although the difference was only significant when comparing NCD-O ($40 \pm 7 \times 10^3$ cells/cm^2) with UNCD substrates ($27 \pm 7 \times 10^3$ cells/cm^2 on UNCD-O and $29 \pm 6 \times 10^3$ cells/cm^2 on UNCD-H). Furthermore, we analyzed nucleus area and nucleus aspect ratio as indicators of cell expansion and shape (see Figures S6-S7, Supporting Information). In the case of full coverage of the surface at high confluency, as it is for BMSCs, the nucleus area was inversely proportional to the cell number. Thus, BMSCs cultured on NCD-O developed significantly smaller nuclei than on the other substrates except for titanium, where the dimensions were similar (303 ± 6 µm^2 for Ti and 291 ± 6 µm^2 for NCD-O). Interestingly, BMSCmax cultured on titanium displayed nuclei with larger aspect ratio compared with cells on diamond-coated substrates, i.e., higher cell elongation on titanium than on diamond coatings. This cannot be solely attributed to the dense cell packing due to confluency since we observed higher number of cells on NCD-O than on titanium. The cell number, nucleus area and nucleus aspect ratio values for BMSCs from BMSCbeh donor where comparable among all substrates (Figure S5-S7,

Supporting Information). Since focal adhesion (FA) of a cell are molecular assemblies that connect the cell to the ECM deposited on the underlying substrate, we examined whether FA assembly would differ between substrates as an additional indicator of cell-substrate interaction and attachment. For visualization of FAs, cells were immunostained to detect vinculin, an integral cytoskeletal protein of FA that links F-actin to the membrane at sites of cell-substrate anchoring. Immunostaining in BMSCs revealed diffused staining through the cytoplasm and bright patches of vinculin at converging sites of F-actin bundles with the membrane at the basal side of the cells cultured on all substrates, with no apparent distinction between substrates (Figure S8, Supporting Information). Therefore, all substrates supported to a similar extend the formation of FA and thus anchoring of BMSCs to the surface.

The surface coverage by the Saos-2 cell population was slightly larger on UNCD-H than on the other substrates (Figure 3b-c). However, no statistically significant differences were obtained. Regarding morphology, the osteogenic Saos-2 cells appeared smaller in size on NCD films and UNCD-O than on UNCD-H and titanium. Analysis of nuclei areas revealed no statistically significant differences when comparing means and medians between different substrates (Figure S6, Supporting Information). However, the size distribution of nuclei areas for Saos-2 on NCD films and UNCD-O is considerably narrower than on the other substrates, with mean and median values below 290 μm^2. In contrast, the mean nucleus area of Saos-2 cultured on titanium was 327 ± 20 μm^2. This suggests better cell attachment and expansion of Saos-2 on titanium and UNCD-H than on oxygen terminated diamond films counterparts. In addition, Saos-2 cells developed a polygonal shape with abundant F-actin bundles along the cell periphery on titanium, UNCD films and NCD-H. In contrast, Saos-2 exhibited an oval to spindle-like shape when cultured on NCD-O. These observations were corroborated by analysis of nuclei aspect ratio

(Figure S7, Supporting Information); Saos-2 cells cultured on NCD-O displayed elongated nuclei with mean aspect ratio value of 1.77 ± 0.05, whereas on titanium the value was significantly smaller (1.54 ± 0.03, $p < 0.001$). Vinculin staining showed assembly of FA at F-actin vertices in the basal side of the cell, particularly at the cell's periphery (Figure S8, Supporting Information). Cytoskeleton organization and FA spatial distribution were comparable for cells plated on titanium and UNCD films. However, cells cultured on NCD films displayed divergent features. As mentioned above, cells cultured on NCD-O exhibited two main morphologies; spindle-like and polygonal. The vinculin staining in spindle-like Saos-2 was rather diffused throughout the cell body with no clear accumulation at F-actin vertices, suggesting inefficient formation of FA. Polygonal-shaped Saos-2 on NCD-O displayed similar cytoskeleton organization, including FAs, as observed on titanium and UNCD films. Saos-2 cultured on NCD-H developed a polygonal shape with bright vinculin patches at F-actin vertices in the cell's periphery and at the poles and across the dorsal surface of the nucleus in polarized cells. FAs in the proximity of the nucleus are associated to the actin cap and are bigger in size and more elongated than other ventral FAs [56]. In addition, FAs coupled to the actin cap are more sensitive to mechanotransduction than other FAs [56] and the actin cap is associated with persistent cell migration [57]. Therefore, Saos-2 cultured on NCD-H might be more migratory active than on the other substrates. It is important to note that FA assembly, maturation and disassembly depends on mechanical tension generated, sensed and transmitted by actomyosin contractibility. FAs are generally viewed as anchoring sites for stagnated cells. However, FAs are also essential for generation of traction forces during migration [58]. Overall, attachment and grow of Saos-2 seemed to excel on titanium and UNCD-H.

Cell confluency for fibroblasts was higher on titanium and UNCD-O compared with other diamond films, with poorest attachment observed for hydrogenated surfaces (Figure 3a-b). Indeed, the number of cells on UNCD-O at day 5 was significantly higher ($p < 0.001$) than on titanium ($22 \pm 3 \times 10^3$ cells/cm^2 and $15 \pm 2 \times 10^3$ cells/cm^2, respectively) and on hydrogen terminated films ($10 \pm 3 \times 10^3$ cells/cm^2 on UNCD-H and $2 \pm 1 \times 10^3$ cells/cm^2 on NCD-H). On NCD-H, cells tended to grow in highly packed cell cluster, i.e., colonies, rather than single, spindle-shaped cells with long F-actin bundles across the cytoplasm as observed on titanium and oxygen terminated films. This was further validated with the analysis of nuclei areas (Figure S6, Supporting Information); fibroblasts cultured on NCD-H developed significantly smaller nuclei when compared to titanium and NCD-O (266 ± 13 μm^2, 374 ± 9 μm^2 and 357 ± 10 μm^2, respectively). Nuclei of fibroblast on UNCD films were also smaller than on titanium, although not statistically significant (323 ± 19 μm^2 on UNCD-O and 336 ± 31 μm^2 on UNCD-H). Furthermore, fibroblasts on NCD-H displayed a wide distribution of nucleus aspect ratio values ranging from 1.23 to 2.57 (1.82 ± 0.11), whereas on titanium and UNCD-H the value ranges were 1.55 - 1.96 (1.78 ± 0.04) and 1.47 - 1.75 (1.71 ± 0.04), respectively. These data demonstrate that fibroblasts on hydrogen terminated diamond were rather small when compared to fibroblasts cultured on titanium, indicating poor cell attachment. In addition, immunostaining revealed diffuse cytoplasmic localization of vinculin with bright patches at F-actin vertices, particularly at lamellipodia in the leading edge of polarized, migratory cells. FAs seemed to be less abundant and weaker in fluorescence signal in fibroblasts cultured on hydrogenated films and NCD-O than on titanium and UNCD-O. Taken together, titanium and UNCD-O were advantageous for attachment and grow of fibroblasts, while hydrogen terminated diamond films were not.

Fibroblasts are the primary source of ECM, which includes fibronectin, laminins, and collagen matrix. These matrix-producing cells can adhere to and grow on any of the aforementioned proteins. However, cell adhesion forces and proliferation rates are higher on fibronectin than on laminin and collagen [59]. In addition, fibronectin adsorption is favored on hydrophilic surfaces while laminin and collagen adsorb better onto hydrophobic ones [59]. Therefore, the poor cell growth observed for fibroblasts on hydrogen-terminated diamond films may be explained by low fibronectin adsorption and disruption of its active conformation as shown by Baujard-Lamotte et al. [60] for adsorption of fibronectin on hydrophobic polystyrene. In contrast, Saos-2 and BMSCs grow preferentially on collagen. However, wettability alone cannot explain cell behavior since fibroblasts grew better on UNCD-H than on NCD-H surface both of which have similar contact angle values (64.9 ± 3.1° and 70.4 ± 3.0°). Thus, surface roughness may also influence fibronectin 3D structure as observed for BSA.

Taken together, UNCD-H and NCD-H appear to be excellent candidate coatings for orthopedic implants since both support colonization of BMSCs and osteogenic cells as well as medical grade titanium. In addition, fibroblasts showed lower colonization on hydrogen terminated diamond than on titanium. This may help prevent implant failure due to the development of fibrosis [61, 62], which is driven by uncontrolled growth of fibroblasts and their transformation to myofibroblasts, leading to excess deposition of pathological ECM around the implant. In this regard, it has been shown that released metal particles generated by mechanical loading in metal-on-metal hip implants are able to activate synovial fibroblasts. This leads to abnormal deposition of ECM, fibrosis and ultimately implant failure [63]. Diamond coating of metal-on-metal implants could prevent or minimize the release of metal and/or diamond wear particles due to its excellent resistance and wear properties. Even though diamond particles may be released, some

studies suggest that diamond nano/microparticles have low cytotoxicity [64, 65]. Although promising, these results should be taken with care. Further *in-vitro* analyses are needed to investigate growth and activation of synovial fibroblasts, ECM deposition and release of wear particles from diamond-coated implants.

4. CONCLUSIONS

In this work, for the first time, we demonstrated deposition of NCD at low temperatures (~400 °C) on three types of acetabular shells each having different surface structure and porosity showing high potential of surface wave plasma CVD technique for coating orthopaedic implants. Coatings on all acetabular shells uniformly covered high and low porosity structures present on the surface. The entire surface of each shell was covered with NCD apart from random regions where diamond films contained small voids or showed signs of delayed nucleation attributed to imperfect seeding density. Furthermore, homogeneous NCD and UNCD coatings were also deposited on titanium hemispheres purposely chosen to mimic the shape of acetabular shells. The biocompatibility of the coatings was assessed by investigating the adsorption of albumin and Type I collagen, and monitoring in real time the proliferation of primary adult fibroblasts, osteogenic cells Saos-2 and bone marrow-derived MSCs. By measuring fluorescence lifetimes, we studied the conformational changes of albumin showing that the surface topology of diamond has a pronounce effect on the structure of adsorbed albumin. Results obtained for collagen indicate that the hydrophilicity of a diamond surface can yield higher mobility and reduced structural stability of collagen. Lastly, we found that hydrogen terminated UNCD and NCD support the colonization of MSCs and osteogenic cells and diminish the colonization of fibroblasts compared to titanium. The proliferation of osteogenic cells on hydrogenated UNCD

was found to be better than on its oxygen terminated counterpart, indicating possible correlation with observed behavior of adsorbed collagen. Biocompatibility assessment shows that surface topology and chemistry of diamond plays profound role in adsorption of proteins and cell proliferation. The results for hydrogenated diamond films show that this type of coating has a great potential being an excellent candidate for orthopaedic implants.

ASSOCIATED CONTENT

Supporting Information

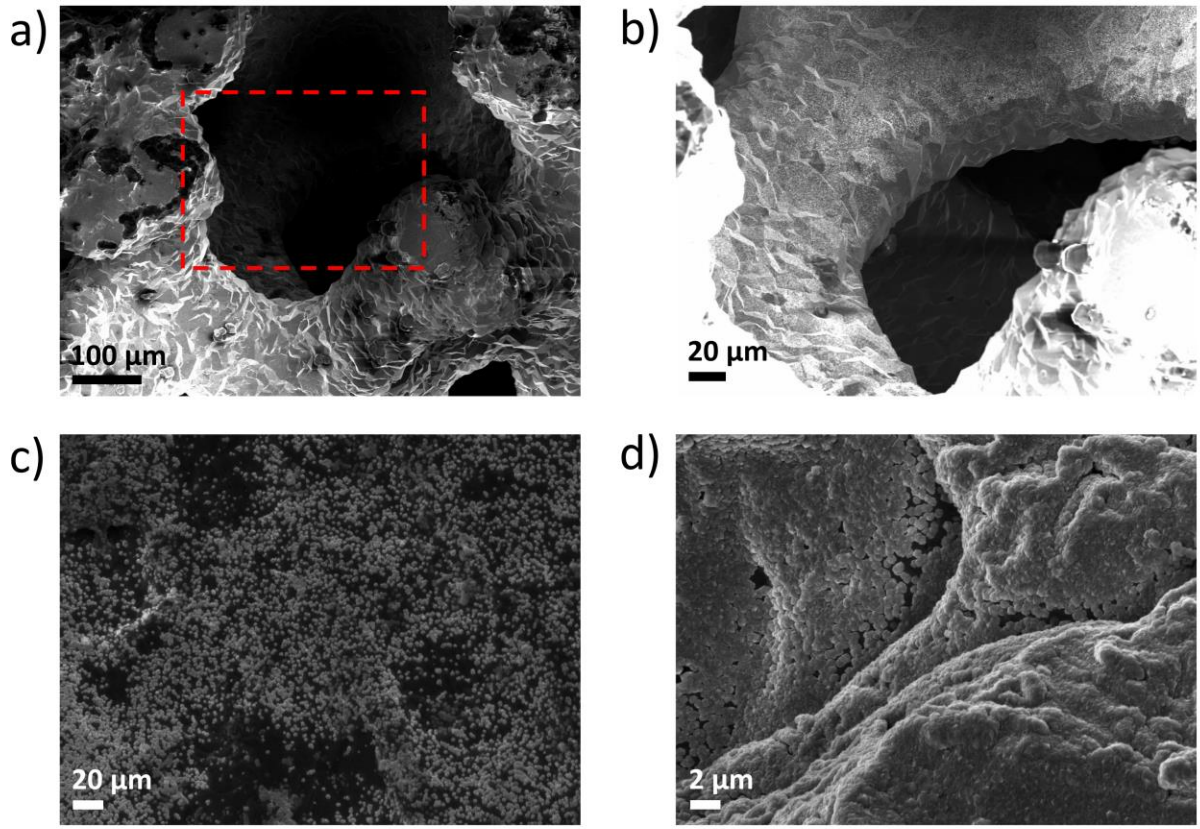

Figure S1. (a, b) Scanning electron micrographs (SEM) of nanocrystalline diamond (NCD) coating on TRABECULAR acetabular shell. Dashed red line indicates area depicted in (b). (c) SEM micrograph of NCD coating on M-MESH acetabular shell illustrating delayed nucleation and growth of diamond. (d) SEM micrograph of voids observed in NCD coating on TRIDENT acetabular shell.

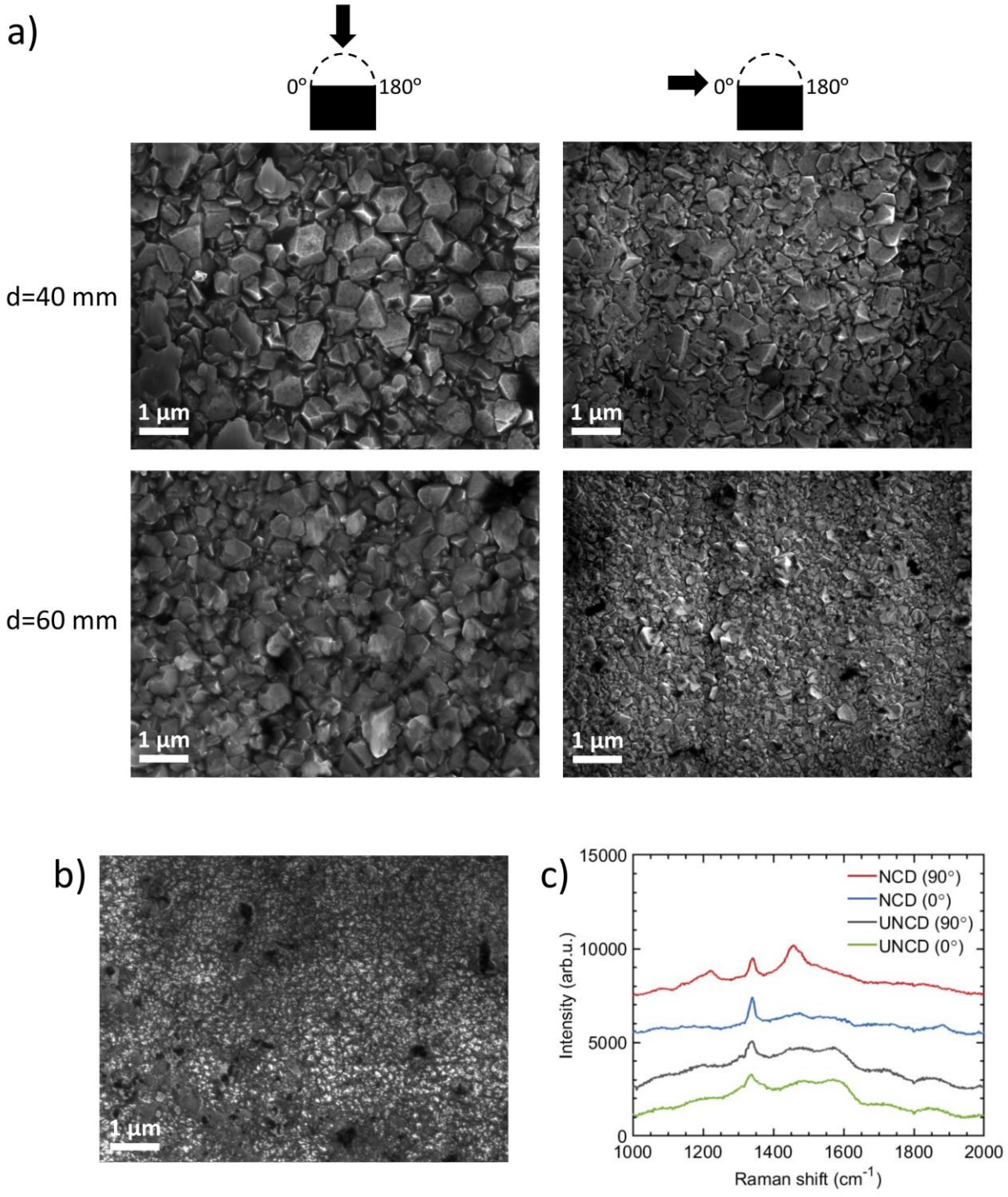

Figure S2. (a) Scanning electron micrographs (SEM) of nanocrystalline diamond NCD on titanium hemispheres showing granularity of coatings at 0 ° and 90 °. (b) SEM micrograph of ultrananocrystalline diamond (UNCD) coating on titanium hemisphere. (c) The background corrected Raman spectra of NCD and UNCD coatings on titanium hemispheres.

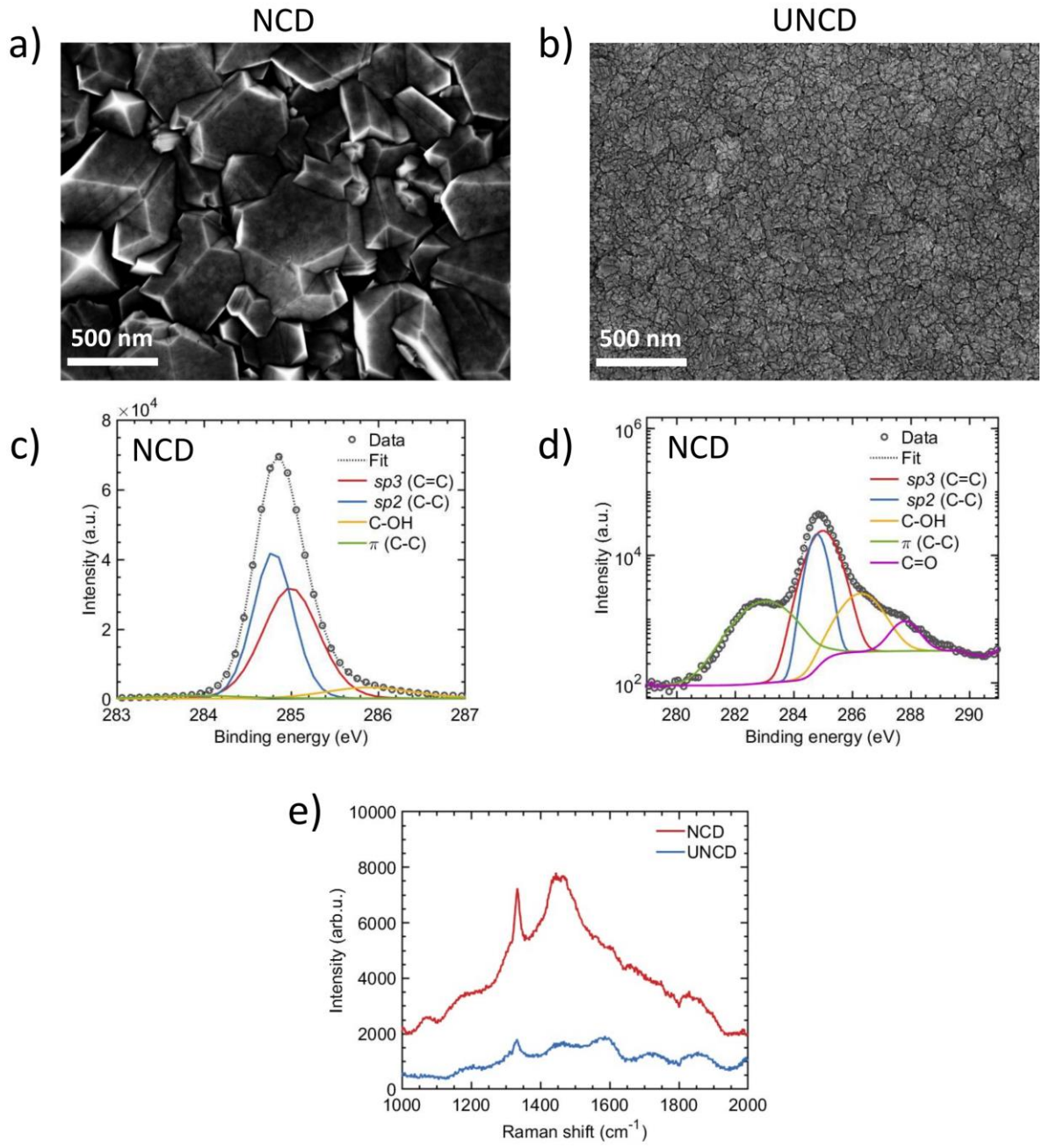

Figure S3. Scanning electron micrographs (SEM) of (a) nanocrystalline diamond (NCD) and (b) ultrananocrystalline diamond (UNCD) films on silicon wafers. Deconvoluted C 1s (carbon) high-resolution X-ray photoelectron spectra (XPS) of (c) hydrogenated and (d) oxygenated NCD film showing peaks fitted for sp3, sp2, C−OH, C=O bonds and π-bonded C atoms. (e) The background corrected Raman spectra of NCD and UNCD films on silicon wafers.

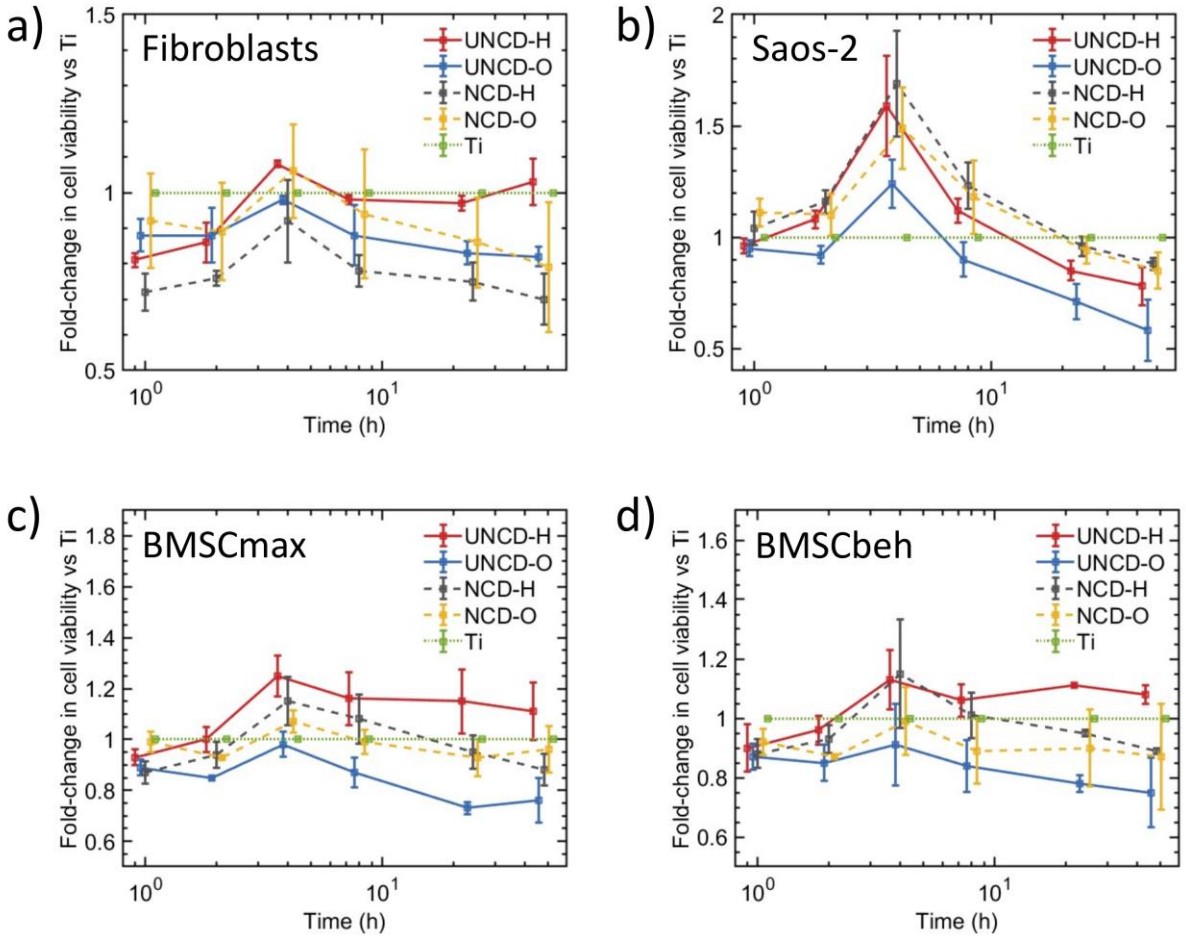

Figure S4. Fold-change in the evolution of luminescence signal versus titanium substrate for (a) fibroblasts, (b) osteosarcoma cell line (Saos-2), (c) human bone marrow-derived mesenchymal stem cells (BMSCmax) and BMSCbeh. Data points are spread around nominal values for better representation of error bars.

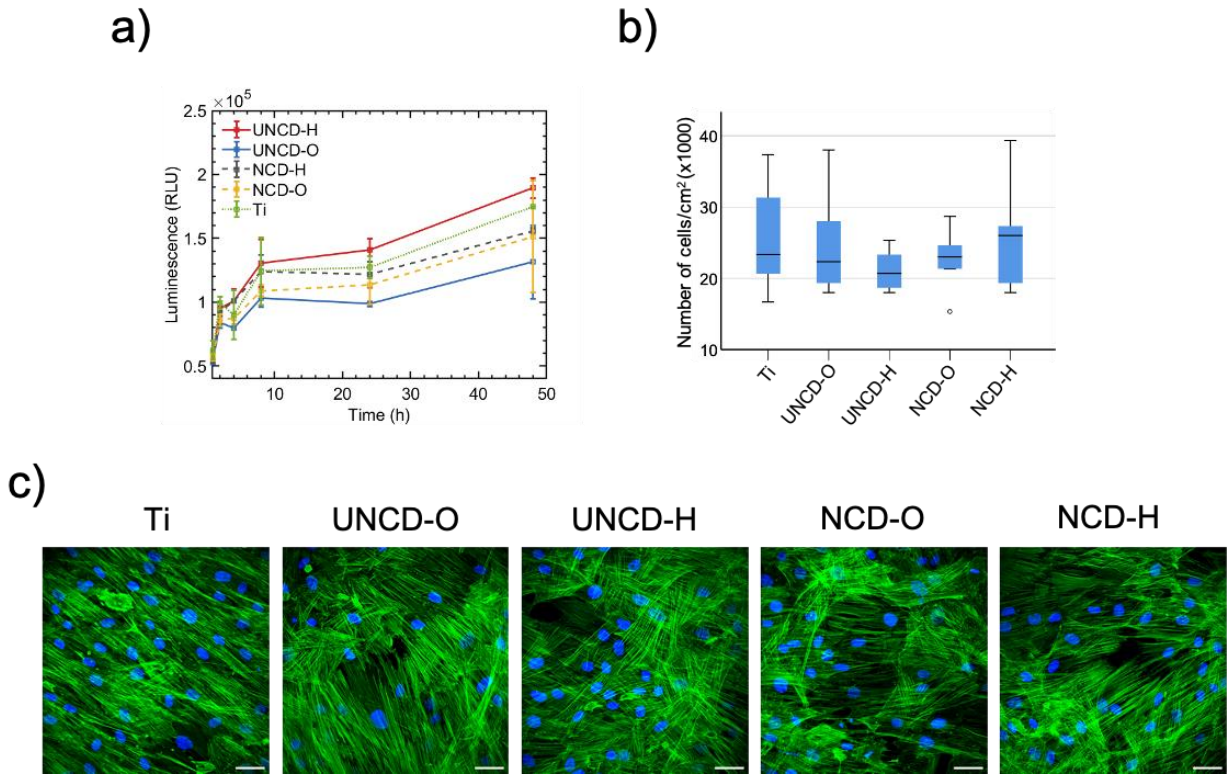

Figure S5. Growth of bone marrow-derived mesenchymal stem cells (BMSCbeh) on titanium and diamond-coated substrates. (a) Evolution in luminescence signal as a measurement of increasing metabolic activity. (b) Number of cells per cm² at day 5 of culture. (c) Fluorescence micrographs of cells fixed at day 5 and stained with phalloidin-ATTO 565 (green) and DAPI (blue) to visualize actin filaments (F-actin) and nuclei, respectively. Shown are maximum z-projections of merged phalloidin-ATTO 565/DAPI. Scale bars are 50 µm.

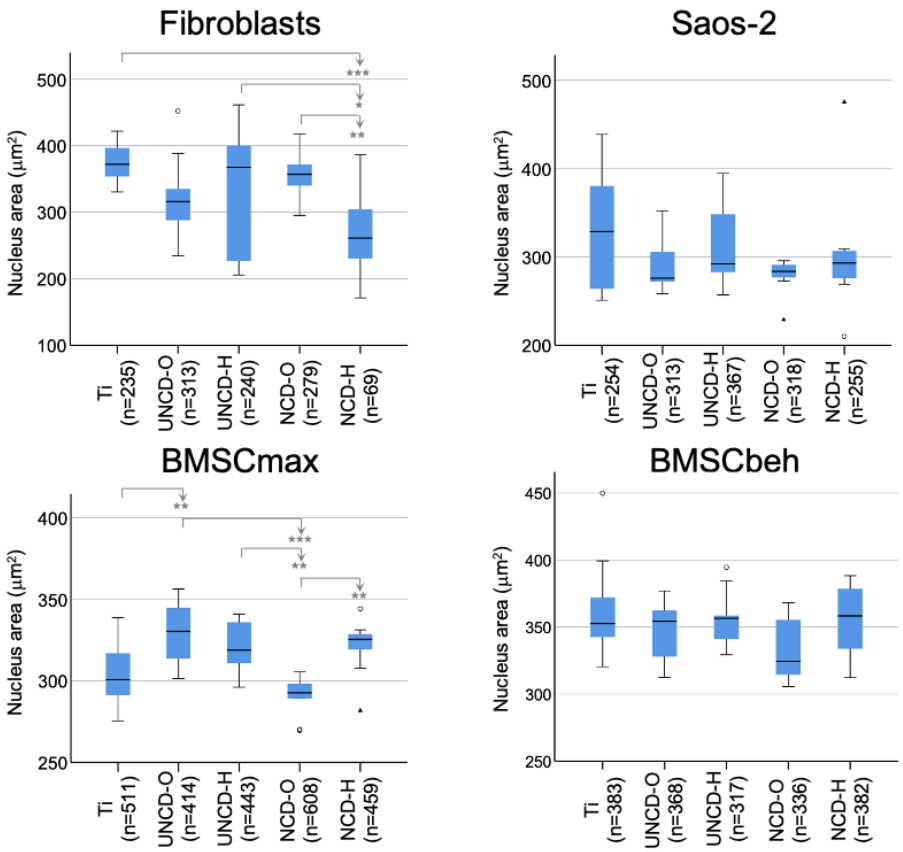

Figure S6. Nucleus area of cells at day 5 of culture on titanium and diamond films. The number of cells analyzed in each condition is enclosed in parenthesis. Statistical annotations: `*' 0.05>p>0.01, `' 0.01>p>0.001, `***' p<0.001.*

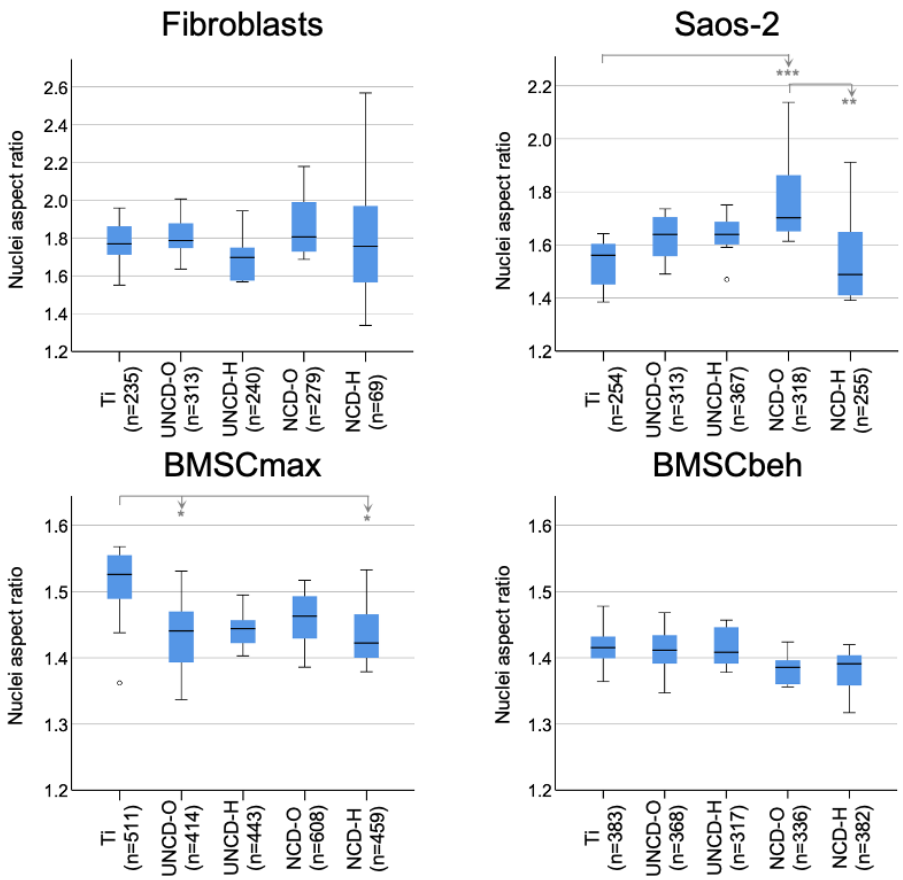

Figure S7. Nuclei aspect ratio of cells at day 5 of culture on titanium and diamond films. The number of cells analyzed in each condition is enclosed in parenthesis. Statistical annotations: `*' 0.05>p>0.01, `' 0.01>p>0.001, `***' p<0.001.*

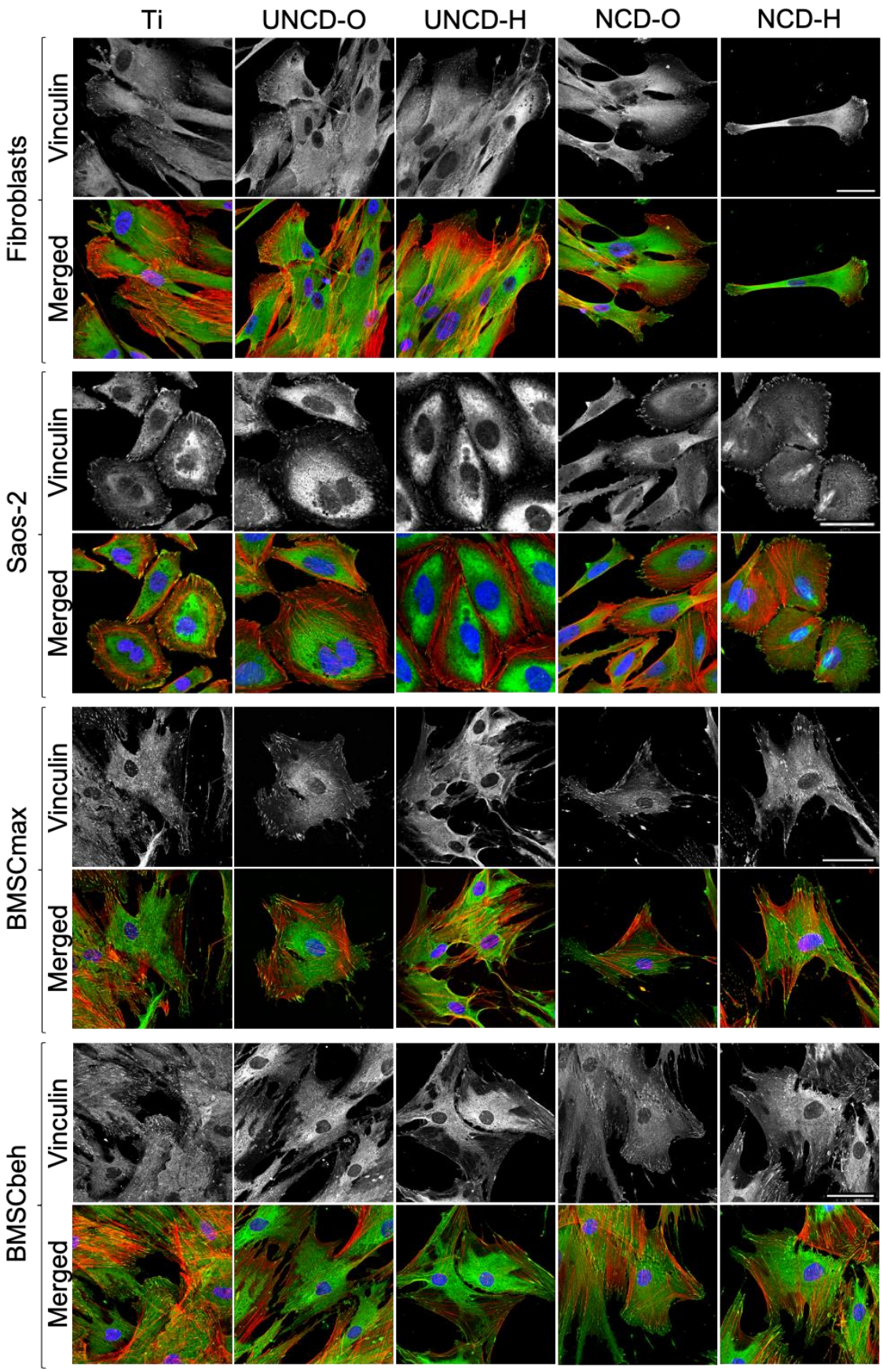
Ti
UNCD-O
UNCD-H
NCD-O
NCD-H
Fibroblasts
Saos-2
BMSCmax
BMSCbeh
Vinculin
Merged

Figure S8. Fluorescence micrographs of cells growing on titanium and diamond films. Cells were fixed at day 5 and immunostained for vinculin (green) and counterstained with phalloidin-ATTO 565 (red) and DAPI (blue) to visualize the actin filaments (F-actin) and nuclei, respectively. Shown are maximum z-projections of merged and single vinculin channels. Scale bars are 50 um.

AUTHOR INFORMATION

Corresponding Author

Justas Zalieckas - Department of Physics and Technology, University of Bergen, Allegaten 55, Bergen, Norway; https://orcid.org/0000-0002-6717-5214; Email: justas.zalieckas@uib.no

Authors

Ivan R. Mondragon - Department for Clinical Dentistry, University of Bergen, Årstadveien 19, Bergen, Norway; https://orcid.org/0000-0001-6819-0718

Paulius Pobedinskas - Institute for Materials Research (IMO), Hasselt University, Wetenschapspark 1, 3590 Diepenbeek, Belgium; IMOMEC, IMEC vzw, Wetenschapspark 1, 3590 Diepenbeek, Belgium; https://orcid.org/0000-0001-8136-5172

Arne S. Kristoffersen - Department of Physics and Technology, University of Bergen, Allegaten 55, Bergen, Norway; https://orcid.org/0000-0002-8327-196X

Samih Mohamed-Ahmed - Department for Clinical Dentistry, University of Bergen, Årstadveien 19, Bergen, Norway; https://orcid.org/0000-0002-2909-8895

Cecilie Gjerde - Department for Clinical Dentistry, University of Bergen, Årstadveien 19, Bergen, Norway; https://orcid.org/0000-0002-7581-6413

Paul J. Høl - Department of Orthopaedic Surgery, Haukeland University Hospital, Jonas Lies vei 65, Bergen, Norway; Department of Clinical Medicine, University of Bergen, Jonas Lies vei 87, Bergen, Norway; https://orcid.org/0000-0002-4216-7891

Geir Hallan - Department of Orthopaedic Surgery, Haukeland University Hospital, Jonas Lies vei 65, Bergen, Norway; Department of Clinical Medicine, University of Bergen, Jonas Lies vei 87, Bergen, Norway; https://orcid.org/0000-0002-8202-3462

Ove N. Furnes - Department of Orthopaedic Surgery, Haukeland University Hospital, Jonas Lies vei 65, Bergen, Norway; Department of Clinical Medicine, University of Bergen, Jonas Lies vei 87, Bergen, Norway; https://orcid.org/0000-0001-8223-2515

Mihaela Roxana Cimpan - Department for Clinical Dentistry, University of Bergen, Årstadveien 19, Bergen, Norway; https://orcid.org/0000-0003-2029-3173

Ken Haenen - Institute for Materials Research (IMO), Hasselt University, Wetenschapspark 1, 3590 Diepenbeek, Belgium; IMOMEC, IMEC vzw, Wetenschapspark 1, 3590 Diepenbeek, Belgium; https://orcid.org/0000-0001-6711-7367

Bodil Holst - Department of Physics and Technology, University of Bergen, Allegaten 55, Bergen, Norway; https://orcid.org/0000-0001-6809-2579

Martin M. Greve - Department of Physics and Technology, University of Bergen, Allegaten 55, Bergen, Norway; https://orcid.org/0000-0003-2309-273X

Funding Sources

This work was financially supported by the Methusalem NANO network.

Notes

The authors declare no competing financial interest.

ACKNOWLEDGMENT

The Research Council of Norway is acknowledged for the support to the Norwegian Micro- and Nano-Fabrication Facility, NorFab, project number 295864 and NanoBioReal, project number 288768.

REFERENCES

[1] Bayliss, L. E.; Culliford, D.; Monk, A. P.; Glyn-Jones, S.; Prieto-Alhambra, D.; Judge, A.; Cooper, C.; Carr, A. J.; Arden, N. K.; Beard, D. J.; Price, A. J. The effect of patient age at intervention on risk of implant revision after total replacement of the hip or knee: a population-based cohort study. *Lancet* **2017**, 389 (10077), 1424-1430. Doi: 10.1016/S0140-6736(17)30059-4

[2] Ferraris, S.; Venturello, A.; Miola, M.; Cochis, A.; Rimondini, L.; Spriano, S. Antibacterial and bioactive nanostructured titanium surfaces for bone integration. *Appl. Surf. Sci.* **2014**, 311, 279-291. Doi: 10.1016/j.apsusc.2014.05.056

[3] Chouirfa, H.; Bouloussa, H.; Migonney, V.; Falentin-Daudré, C. Review of titanium surface modification techniques and coatings for antibacterial applications. *Acta Biomater*. **2019**, 83, 37-54. Doi: 10.1016/j.actbio.2018.10.036

[4] Singh, G.; Agrawal, K.; Singh, S.; Satya, P. Hydroxyapatite Coating for BioImplants and Problem Associated with Coating Techniques: A Review, **2010**.

[5] Hussain, M.; Askari Rizvi, S. H.; Abbas, N.; Sajjad, U.; Shad, M. R.; Badshah, M.A.; Malik, A. I. Recent Developments in Coatings for Orthopedic Metallic Implants. *Coatings* **2021**, 11 (7), 791. Doi: 10.3390/coatings11070791

[6] Fong, J. S.; Booth, M. A.; Rifai, A.; Fox, K.; Gelmi, A. Diamond in the Rough: Toward Improved Materials for the Bone-Implant Interface. *Adv. Healthc. Mater.* **2021**, 10 (14), 2100007. Doi: 10.1002/adhm.202100007

[7] Pareta, R.; Yang, L.; Kothari, A.; Sirinrath, S.; Xiao, X.; Sheldon, B.W.; Webster, T.J. Tailoring nanocrystalline diamond coated on titanium for osteoblast adhesion. *J. Biomed. Mater. Res. A*. **2010**, 95 (1), 129-136. Doi: 10.1002/jbm.a.32821

[8] Yang, L.; Sheldon, B.W.; Webster, T. J. The impact of diamond nanocrystallinity on osteoblast functions. *Biomaterials* **2009**, 30 (20), 3458-3465. Doi: 10.1016/j.biomaterials.2009.03.014

[9] Rezek, B.; Michalíková, L.; Ukraintsev, E.; Kromka, A.; Kalbacova, M. Micro-pattern guided adhesion of osteoblasts on diamond surfaces. *Sensors* **2009**, 9 (5), 3549-3562. Doi: 10.3390/s90503549

[10] Jakubowski, W.; Bartosz, G.; Niedzielski, P.; Szymanski, W.; Walkowiak, B. Nanocrystalline diamond surface is resistant to bacterial colonization. *Diam. Relat. Mater.* **2004**, 13 (10), 1761-1763. Doi: 10.1016/j.diamond.2004.03.003

[11] Rifai, A.; Tran, N.; Reineck, P.; Elbourne, A.; Mayes, E.; Sarker, A.; Dekiwadia, D.; Ivanova, E. P.; Crawford, R. J.; Ohshima, T.; Gibson, B. C.; Greentree, A. D.; Pirogova, E.; Fox, K. Engineering the interface: nanodiamond coating on 3D-printed titanium promotes mammalian

cell growth and inhibits Staphylococcus aureus colonization. *ACS appl. mater. Inter.* **2019**, 11 (27), 24588-24597. Doi: 10.1021/acsami.9b07064

[12] Skoog, S. A.; Kumar, G.; Zheng, J.; Sumant, A. V.; Goering, P. L.; Narayan, R. J. Biological evaluation of ultrananocrystalline and nanocrystalline diamond coatings. *J. Mater. Sci-Mater. M.* **2016**, 27 (12), 1-13. Doi: 10.1007/s10856-016-5798-y

[13] Maru, M.M.; Amaral, M.; Rodrigues, S.P.; Santos, R.; Gouvea, C.P.; Archanjo, B.S.; Trommer, R.M.; Olivera, F. J.; Silva, R.F.; Achete, C. A. The High performance of nanocrystalline CVD diamond coated hip joints in wear simulator test. *J. Mech. Behave. Biomed.* **2015**, 49, 175-185. Doi: 10.1016/j.jmbbm.2015.05.005

[14] Gracio, J.J.; Fan, Q.H.; Madaleno, J.C. Diamond growth by chemical vapour deposition. *J Phys. D. Appl. Phys*. **2010**, 43 (37), 374017. Doi: 10.1088/0022-3727/43/37/374017

[15] Humin, L.; Dandy, D.S. *Diamond Chemical Vapor Deposition: Nucleation and Early Growth Stages*; William Andrew Publishing, 1995.

[16] Narayan, R. *Diamond-Based Materials for Biomedical Applications*; Woodhead Publishing Series in Biomaterials, 2013.

[17] Zalieckas, J.; Pobedinskas, P.; Greve, M.M.; Eikehaug, K.; Haenen, K.; Holst, B. Large area microwave plasma CVD of diamond using composite right/left-handed materials. *Diam. Relat. Mater*. **2021**, 116, 108394. Doi: 10.1016/j.diamond.2021.108394

[18] Rifai, A.; Tran, N.; Lau, D.W.; Elbourne, A.; Zhan, H.; Stacey, A.D.; Mayes, E.L.H.; Sarker, A.; Ivanova, E.P.; Crawford, R.J.; Tran, P.A.; Gibson, B.C.; Greentree, A.D.; Pirogova,

E.; Fox, K. Polycrystalline diamond coating of additively manufactured titanium for biomedical applications. *ACS Appl. Mater. Inter*. **2018**, 10 (10), 8474-8484. Doi: 10.1021/acsami.7b18596

[19] Aaqil, R.; Creedon, D.; Tran, N.; Hejazi, M.; Garrett, D.; Greentree, A.D.; Pirogova, E.; Stacey, A.; Fox, K. Highly uniform polycrystalline diamond coatings of three-dimensional structures. *Surface and Coatings Technology* **2021**, 408, 126815. Doi: 10.1016/j.surfcoat.2020.126815

[20] Mehedi, H.A.; Achard, J.; Rats, D.; Brinza, O.; Tallaire, A.; Mille, V.; Silva, F.; Provent, Ch.; A. Gicquel. Low temperature and large area deposition of nanocrystalline diamond films with distributed antenna array microwave-plasma reactor. *Diam. Relat. Mater*. **2014**, 47, 58-65. Doi: 10.1016/j.diamond.2014.05.004

[21] Kim, J.; Tsugawa, K.; Ishihara, M.; Koga, Y.; Hasegawa, M. Large-area surface wave plasmas using microwave multi-slot antennas for nanocrystalline diamond film deposition. *Plasma Sources Sci. T.* **2009**, 19 (1), 015003. Doi: 10.1088/0963-0252/19/1/015003

[22] Izak, T.; Babchenko, O.; Varga, M.; Potocky, S.; Kromka, A. Low temperature diamond growth by linear antenna plasma CVD over large area. *Phys. Status Solidi B.* **2012**, 249 (12), 2600-2603. Doi: 10.1002/pssb.201200103

[23] Tsugawa, K.; Ishihara, M.; Kim, J.; Koga, Y.; Hasegawa, M. Nanocrystalline diamond film growth on plastic substrates at temperatures below 100 C from low-temperature plasma. *Phys. Rev. B*. **2010**, 82 (12), 125460. Doi: 10.1103/PhysRevB.82.125460

[24] Dekkar, D.; Bénédic, F.; Falentin-Daudré, C.; Brinza, O.; Issaoui, R.; Achard, J. Investigation of a distributed antenna array microwave system for the three-dimensional low-

temperature growth of nanocrystalline diamond films. *Diam. Relat. Mater*. **2019**, 94, 28-36. Doi: 10.1016/j.diamond.2019.02.016

[25] Varga, M.; Potocky, S.; Tesarek, P.; Babchenko, O.; Davydova, M.; Kromka, A. Diamond growth on copper rods from polymer composite nanofibres. *Appl. Surf. Sci*. **2014**, 312, 220-225. Doi: 10.1016/j.apsusc.2014.05.083

[26] Alcaide, M.; Papaioannou, S.; Taylor, A.; Fekete, L.; Gurevich, L.; Zachar, V.; Pennisi, C.P. Resistance to protein adsorption and adhesion of fibroblasts on nanocrystalline diamond films: the role of topography and boron doping. *J. Mater. Sci.: Mater. Med.* **2016**, 27 (90). Doi: 10.1007/s10856-016-5696-3

[27] Amaral, M.; Gomes, P.S.; Lopes, M.A.; Santos, J.D.; Silva, R.F.; Fernandes, M.H. Cytotoxicity evaluation of nanocrystalline diamond coatings by fibroblast cell cultures. *Acta Biomaterialia* **2009**, 5 (2), 755-763. Doi: 10.1016/j.actbio.2008.08.015

[28] Liskova, J.; Babchenko, O.; Varga, M.; Kromka, A.; Hadraba, D.; Svindrych, Z.; Burdikova, Z.; Bacakova, L. Osteogenic cell differentiation on H-terminated and O-terminated nanocrystalline diamond films. *Int. J. Nanomedicine* **2015**, 10 (1), 869-884. Doi: 10.2147/IJN.S73628

[29] Rifai, A.; Tran, N.; Leitch, V.; Booth, M.A., Williams, R.; Fox, K. Osteoblast Cell Response on Polycrystalline Diamond-Coated Additively Manufactured Scaffolds. *ACS Appl. Bio Mater.* **2021**, 4 (10) 7509-7516. Doi: 10.1021/acsabm.1c0075

[30] Clem, W.C.; Chowdhury, S.; Catledge, S.A.; Weimer, J.J.; Shaikh, F.M.; Hennessy, K.M.; Konovalov, V.V.; Hill, M.R.; Waterfeld, A.; Bellis, S.L.; Vohra, Y.K. Mesenchymal stem cell

interaction with ultra-smooth nanostructured diamond for wear-resistant orthopaedic implants. *Biomaterials* **2008**, 29 (24-25), 3461-3468. Doi: 10.1016/j.biomaterials.2008.04.045

[31] Pobedinskas, P.; Degutis, G.; Dexters, W.; D'Haen, J.; Van Bael, M.K.; Haenen, K. Nanodiamond seeding on plasma-treated tantalum thin films and the role of surface contamination. *Appl. Surf. Sci*. **2021**, 538, 148016. Doi: 10.1016/j.apsusc.2020.148016

[32] Degutis, G.; Pobedinskas, P.; Boyen, H.G.; Dexters, W.; Janssen, W.; Drijkoningen, S.; Hardy, A.; Haenen, K.; Van Bael, M.K. Improved nanodiamond seeding on chromium by surface plasma pretreatment. *Chem. Phys. Lett.* **2015**, 640, 50-54. Doi: 10.1016/j.cplett.2015.10.002

[33] Williams, O.A.; Douhéret, O.; Daenen, M., Haenen, K.; Ōsawa, E.; Takahashi, M. Enhanced diamond nucleation on monodispersed nanocrystalline diamond. *Chem. Phys. Lett.* **2007**, 445 (4-6), 255-258. Doi: 10.1016/j.cplett.2007.07.091

[34] Sun, B.; Zhang, X.; Zhang, Q.; Lin, Z. Effect of atomic hydrogen and oxygen on diamond growth. *J. appl. phys*. **1993**, 73 (9), 4614-4617. Doi: 10.1063/1.352754

[35] Stiegler, J.; Lang, T.; Nyga, M.; Von Kaenel, Y.; Blank, E. Low temperature limits of diamond film growth by microwave plasma-assisted CVD. *Diam. Relat. Mater.* **1996**, 5 (3-5), 226-230. Doi: 10.1016/0925-9635(95)00349-5

[36] Maniotis, A.J.; Chen, C.S.; Ingber, D.E. Demonstration of mechanical connections between integrins, cytoskeletal filaments, and nucleoplasm that stabilize nuclear structure. *Proceedings of the National Academy of Sciences* **1997**, 94 (3), 849-854. Doi: 10.1073/pnas.94.3.849

[37] Versaevel, M.; Grevesse, T.; Gabriele, S. Spatial coordination between cell and nuclear shape within micropatterned endothelial cells. *Nat. Commun.* **2012**, 3, 671. Doi: 10.1038/ncomms1668

[38] Buxboim, A.; Ivanovska, I.L.; Discher, D.E. Matrix elasticity, cytoskeletal forces and physics of the nucleus: how deeply do cells 'feel' outside and in? *J. Cell. Sci.* **2010**, 123 (3), 297-308. Doi: 10.1242/jcs.041186

[39] Rowat, A.C.; Lammerding, J.; Herrmann, H.; Aebi, U. Towards an integrated understanding of the structure and mechanics of the cell nucleus. *Bioessays* **2008**, 30, 226-236. Doi: 10.1002/bies.20720

[40] Rueden, C.T.; Schindelin, J.; Hiner, M.C.; DeZonia, B.E.; Walter, A.E.; Arena, E.T. Eliceiri, K.W. ImageJ2: ImageJ for the next generation of scientific image data. *BMC Bioinformatics* **2017**, 18, 529. Doi: 10.1186/s12859-017-1934-z

[41] Tsugawa, K.; Kawaki, S.; Ishihara, M.; Kim, J.; Koga, Y.; Sakakita, H.; Koguchi, H.; Hasegawa, M. Nanocrystalline diamond growth in a surface-wave plasma. *Diam. Relat. Mater.* **2011**, 20 5-6, 833-838. Doi: 10.1016/j.diamond.2011.03.031

[42] Obrusník, A.; Bonaventura, Z. Studying a low-pressure microwave coaxial discharge in hydrogen using a mixed 2D/3D fluid model. *J. Phys. D. Appl. Phys*. **2015**, 48 (6), 065201. Doi: 10.1088/0022-3727/48/6/065201

[43] Mapelli, C.; Castiglioni, C.; Zerbi, G.; Müllen, K. Common force field for graphite and polycyclic aromatic hydrocarbons. *Phys. Rev. B.* **1999**, 60 (18), 12710. Doi: 10.1103/PhysRevB.60.12710

[44] Ferrari, A.C.; Robertson, J. Origin of the 1150 cm^{-1} Raman mode in nanocrystalline diamond. *Phys. Rev. B.* **2001**, 63 (12), 121405. Doi: 10.1103/PhysRevB.63.121405

[45] Pfeiffer, R.; Kuzmany, H.; Knoll, P.; Bokova, S.; Salk, N.; Günther, B. Evidence for trans-polyacetylene in nano-crystalline diamond films. *Diam. Relat. Mater*. **2003**, 12 (3-7), 268-271. Doi: 10.1016/S0925-9635(02)00336-9

[46] Tsugawa, K.; Ishihara, M.; Kim, J.; Koga, Y.; Hasegawa, M. Nucleation enhancement of nanocrystalline diamond growth at low substrate temperatures by adamantane seeding. *J. Phys. Chem. C.* **2010**, 114 (9), 3822-3824. Doi: 10.1021/jp910555x

[47] Handschuh-Wang, S.; Wang, T.; Druzhinin, S.I.; Wesner, D.; Jiang, X.; Schönherr, H. Detailed study of BSA adsorption on micro-and nanocrystalline diamond/β-SiC composite gradient films by time-resolved fluorescence microscopy. *Langmuir* **2017** 33 (3), 802-813. Doi: 10.1021/acs.langmuir.6b04177

[48] Hungerford, G.; Benesch, J.; Mano, J.F.; Reis, R.L. Effect of the labelling ratio on the photophysics of fluorescein isothiocyanate (FITC) conjugated to bovine serum albumin. *Photoch. Photobio. Sci.* **2007**, 6 (2), 152-158. Doi: 10.1039/B612870J

[49] Norde, W.; Giacomelli, C.E. BSA structural changes during homomolecular exchange between the adsorbed and the dissolved states. *J. Biotechnol*. **2000**, 79 (3), 259-268. Doi: 10.1016/S0168-1656(00)00242-X

[50] Kawarada, H.; Ruslinda, A.R. Diamond electrolyte solution gate FETs for DNA and protein sensors using DNA/RNA aptamers. *Phys. Status Solidi A*. **2011**, 208 (9), 2005-2016. Doi: 10.1002/pssa.201100503

[51] Baler, K.; Martin, O.A.; Carignano, M.A.; Ameer, G.A.; Vila, J.A.; Szleifer, I. Electrostatic unfolding and interactions of albumin driven by pH changes: a molecular dynamics study. *J. Phys. Chem. B.* **2014** 118 (4), 921-930. Doi: 10.1021/jp409936v

[52] Jiang, F.; Hörber, H.; Howard, J.; Müller, D.J. Assembly of collagen into microribbons: effects of pH and electrolytes. *J. Struct. Biol.* **2004**, 148 (3), 268-78. Doi: 10.1016/j.jsb.2004.07.001

[53] Buehler, M.J. Nature designs tough collagen: Explaining the nanostructure of collagen fibrils. *PNAS* **2006**, 103 (33) 12285-12290. Doi: 10.1073/pnas.0603216103

[54] Cole, D.J.; Payne, M.C.; Ciacchi, L.C. Water structuring and collagen adsorption at hydrophilic and hydrophobic silicon surfaces. *Phys. Chem. Chem. Phys.* **2009**, 11, 11395-11399. Doi: 10.1039/B816125A

[55] Somaiah, C.; Kumar, A.; Mawrie, D.; Sharma, A.; Patil, S.D.; Bhattacharyya, J.; Swaminathan, R.; Jaganathan, B.G. Collagen Promotes Higher Adhesion, Survival and Proliferation of Mesenchymal Stem Cells. *PloS one* **2015**, 10 (12). Doi: 10.1371/journal.pone.0145068

[56] Kim, D.H.; Khatau, S.; Feng, Y.; Walcott, S.; Sun, S.X.; Longmore, G.D.; Wirtz, D. Actin cap associated focal adhesions and their distinct role in cellular mechanosensing. *Sci. Rep.* **2012**, 2, 555. Doi: 10.1038/srep00555

[57] Kim, D.H.; Cho, S.; Wirtz, D. Tight coupling between nucleus and cell migration through the perinuclear actin cap. *J. Cell Sci.* **2014**, 127 (11), 2528–2541. Doi: 10.1242/jcs.144345

[58] Hu, Y.L.; Lu, S.; Szeto, K.W.; Sun, J.; Wang, Y.; Lasheras, J.C.; Chien, S. FAK and paxillin dynamics at focal adhesions in the protrusions of migrating cells. *Sci. Rep.* **2014**, 4, 6024. Doi: 10.1038/srep06024

[59] Schlie, S.; Gruene, M.; Dittmar, H.; Chichkov, B.N. Dynamics of cell attachment: adhesion time and force. *Tissue Eng. Part C Methods* **2012**, 18 (9), 688-96. Doi: 10.1089/ten.TEC.2011.0635

[60] Baujard-Lamotte, L.; Noinville, S.; Goubard, F.; Marque, P.; Pauthe, E. Kinetics of conformational changes of fibronectin adsorbed onto model surfaces. *Colloids and Surfaces B: Biointerfaces* **2008**, 63 (1), 129-137. Doi: 10.1016/j.colsurfb.2007.11.015

[61] Ries, M.D.; Badalamente, M. Arthrofibrosis after total knee arthroplasty. *Clin. Orthop. Relat. Res.* **2000**, 380, 177-83. Doi: 10.1097/00003086-200011000-00024

[62] Noskovicova, N.; Hinz, B.; Pakshir, P. Implant Fibrosis and the Underappreciated Role of Myofibroblasts in the Foreign Body Reaction. *Cells* **2021**, 10 (7), 1794. Doi: 10.3390/cells10071794

[63] Xu, J.; Yang, J.; Chen, J.; Zhang, X.; Wu, Y.; Hart, A.; Nyga, A.; Shelton, J.C. Activation of synovial fibroblasts from patients at revision of their metal-on-metal total hip arthroplasty. *Part. Fibre. Toxicol.* **2020**, 17 (42). Doi: 10.1186/s12989-020-00374-y

[64] Schrand, A.M.; Huang, H.; Carlson, C.; Schlager, J.J.; Ōsawa, E.; Hussain, S.M.; Dai, L. Are Diamond Nanoparticles Cytotoxic? *J. Phys. Chem. B* **2007**, 111 (1), 2-7. Doi: 10.1021/jp066387v

[65] Deschatrette, J.; Fougere-Deschatrette, C.; Corcos, L.; Schimke, R.T. Expression of the mouse serum albumin gene introduced into differentiated and dedifferentiated rat hepatoma cells. *PNAS* **1985**, 82 (3) 765-769. Doi: 10.1073/pnas.82.3.765